Monitoring Metabolic Alteration in Cancer Cells upon Radiation Therapy by Surface-Enhanced Raman Scattering (SERS)

by

Xiangyu Chen
B.Sc., University of Victoria, 2021

A Thesis Submitted in Partial Fulfillment
of the Requirements for the Degree of

MASTER OF SCIENCE

in the Department of Chemistry

Supervisory Committee

Monitoring Metabolic Alteration in Cancer Cells upon Radiation Therapy by Surface-Enhanced Raman Scattering (SERS)
by

Xiangyu Chen
B.Sc., from University of Victoria, 2021

Supervisory Committee

Dr. Alexandre G. Brolo, Department of Chemistry
Supervisor

Dr. Peter Loock, Department of Chemistry
Departmental Member

Abstract

Surface-Enhanced Raman Spectroscopy (SERS) is a highly selective and sensitive method that allows the tracking and identification of metabolites at low concentrations in cellular models. In this work, radiation-induced metabolism changes were investigated by SERS using the MCF-7 breast cancer cell line. SERS analysis was carried out on a time course (1, 4, 8, 12-days post exposure) of supernatant samples from MCF-7 cell line cultures previously exposed to either 5 or 20 Gy of ionizing radiation. A significant radiation biomarker, hypoxanthine, was identified through principal component analysis. The amount of hypoxanthine released into the extracellular environment increased over time after exposure to ionizing radiation. A potential mechanism for hypoxanthine production was suggested. Additionally, Caspase-3 inhibitor (Peptide Z-DEVD-FMK) treatment was employed to improve MCF-7 cell viability following exposure to ionizing radiation and to establish the relationship between the release of hypoxanthine and cell apoptosis. This study provides a valuable preliminary assessment of the application of SERS to study metabolic changes that can be extended in the future to human-derived samples.

Table of Contents

List of Figures

Acknowledgments

I am grateful to Dr. Alexandre G. Brolo for providing me with the opportunity to conduct my master's research project under his guidance and for his invaluable support and encouragement throughout.

Additionally, I extend my appreciation to all the colleagues in Dr. Brolo's group for their constructive feedback, helpful discussions, and collaborative work environment, which have enhanced my research experience and expanded my scientific knowledge.

I would also like to thank visiting student Javier Plou from Spain for sharing his cell culture expertise and providing valuable insights into the research field, motivating me to pursue my research goals with dedication and enthusiasm.

Last but not least, I express my gratitude to my family for their unconditional love, patience, and support, which have been my constant source of motivation forever.

Chapter 1. Objectives

Breast cancer is the most diagnosed cancer among women globally. The high sensitivity and specificity of the SERS (Surface-enhanced Raman scattering) technique make it possible to detect subtle changes in the metabolic profile of cancer cells, which can reveal information about the disease progression and treatment response. In this thesis, the SERS technique was used to analyze the metabolites released from the MCF-7 breast cancer cells following radiation therapy. The aim was to gain insight into the underlying mechanisms of irradiated breast cancer cell metabolism and identify potential biomarkers that can be correlated to radiosensitivity. This type of insight can potentially improve patient outcomes and advance the understanding and management of cancer.

This thesis is structured into five chapters. The first chapter outlines the objectives. Chapter 2 provides an overview of the MCF-7 cancer cell line, the mechanism of radiation therapy, the effects of caspase-3 inhibitor on cancer cells, a general review of Raman scattering and SERS mechanism, the principles of coffee ring-based SERS substrates for measurement, and the data analysis method (principal component analysis PCA). Chapter 3 will focus on experimental details, including MCF-7 cell culture, the collection of supernatant samples from irradiated MCF-7 cells, and the use of caspase-3 inhibitor treatment. Additionally, Chapter 3 will include the details of the SERS measurement setup. Chapter 4 will present and analyze the results of the SERS measurements, including the identification of potential biomarkers in cell metabolism and the investigation of biomarker release during cell apoptosis. Finally, Chapter 5 will provide a brief conclusion and outline the future work of this thesis.

Chapter 2. Introductions

2.1 Breast Cancer and MCF-7 Breast Cancer Cell Line

Breast cancer is a serious public health issue that affects millions of people globally. It is the most diagnosed cancer in women and the leading cause of death among women. Breast cancer can occur at any age and is a complex disease that is influenced by a variety of genetic and environmental factors.[1] According to the World Health Organization (WHO), in 2020, there were 2.3 million women diagnosed with breast cancer and 685,000 deaths globally.[2] As of the end of 2020, there were 7.8 million women alive who were diagnosed with breast cancer in the past 5 years, making it the world's most prevalent cancer.[2]

The MCF-7 (Michigan Cancer Foundation-7) cell line is a commonly used breast cancer cell line in the field of cancer research. The cell line was obtained from a patient and was established in 1970 at the Michigan Cancer Foundation.[3]

The MCF-7 cell line has been widely used in a variety of research applications and has made significant contributions to our understanding of the biology of breast cancer and the development of new treatments for this disease. One of the most well-known applications of MCF-7 cells is in the development of anti-cancer drugs.[3,4] Researchers use the MCF-7 cell line to test the ability of new drugs to inhibit the growth and survival of breast cancer cells and investigate the drug action mechanisms. This allows the effectiveness of new drugs to be determined before they are tested in animal models and eventually in human clinical trials. Tengku Din et al. found that rapamycin may play an anticancer role by inhibiting the growth and some morphological changes of MCF-7 cancer cells.[5] Jamalzadeh et al. found that artesunate significantly inhibits the growth of MCF-7

cells in a dose- and time-dependent manner through induction of apoptosis by intrinsic and extrinsic caspase-dependent pathways.[6] MCF-7 cells are classified as hormone receptor-positive breast cancer cells because they express both estrogen receptors (ER) and progesterone receptors (PR).[3] These receptors are proteins located on the surface of cancer cells that can bind to the hormones estrogen and progesterone. In hormone receptor-positive breast cancer, the growth and proliferation of cancer cells are influenced by estrogen and progesterone.[7] The binding of these hormones to their respective receptors can stimulate cell division and promote tumour growth. Consequently, hormone receptor-positive breast cancers tend to exhibit a more indolent behaviour and respond well to hormonal therapies that target the estrogen receptor pathway.[8]

In our experimental studies, we aim to examine the effects of radiotherapy on MCF-7 breast cancer cells. Our experiment will involve culturing the MCF-7 cells in a laboratory setting and exposing them to radiotherapy to induce stress in the MCF-7 cells and assess the extracellular metabolism of resistant cells after exposure. The metabolism of the surviving cells will be our research object. By studying the changes in extracellular metabolism that occur in the surviving cells, we aim to gain a better understanding of the cellular responses to radiotherapy and how these responses may impact the outcome of radiotherapy in patients.

2.2 Radiation Therapy (Radiotherapy)

Radiation therapy, also known as radiotherapy, is a type of cancer treatment that uses high-energy X-rays delivered through a linear accelerator to kill cancer cells. It is a common and effective treatment option for many types of cancer, including breast, lung, prostate, and head and neck cancer. Radiation therapy has a long and rich history dating

back to the late 19th century. The discovery of X-rays by Wilhelm Röntgen in 1895 marked the beginning of the use of ionizing radiation in medicine.[9] Soon after, Marie Curie and Pierre Curie discovered radioactivity and the therapeutic potential of radium.[10] In the early 1900s, the first reported use of radiation therapy for the treatment of cancer was documented, and by the 1920s, the first dedicated radiation therapy departments were established in hospitals.[11]

2.2.1 Mechanisms of Action of Radiation Therapy

Radiation therapy operates through the utilization of the properties of ionizing radiation. This form of energy possesses sufficient power to displace electrons from atoms, thereby forming ions. Its mechanisms of action encompass both direct damage to DNA and indirect DNA damage (shown in **Figure 2.1**).[9, 12] The direct DNA damage is one of the most important mechanisms of action of radiation therapy, which interferes with the cell's ability to divide and grow. Alternatively, by generating free radicals which are derived from the ionization or excitation of the water component (80% of a cell is composed of water) of the cells, ionizing radiation can also cause indirect DNA damage by oxidative dress.[12]

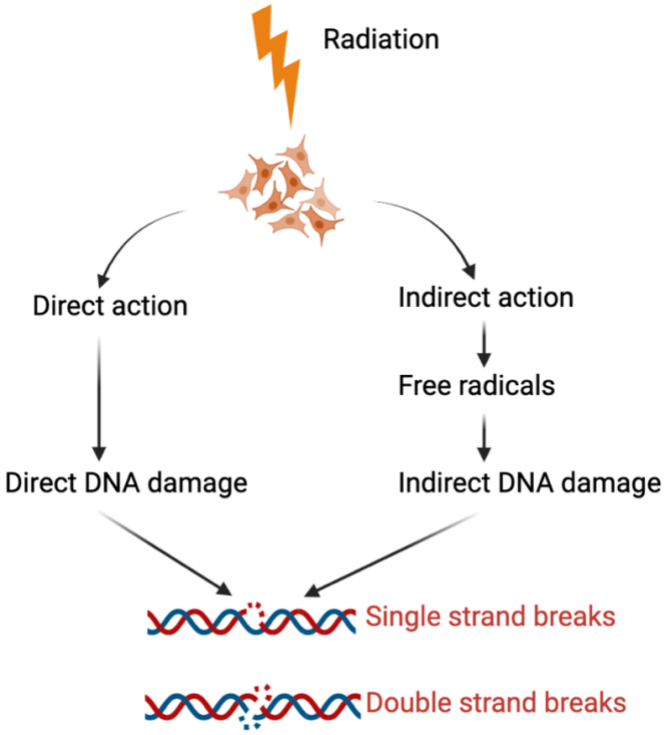

Figure 2.1 Radiation mainly acts in two ways: direct effects and indirect effects.

The mechanism of DNA damage-induced apoptosis involves a complex interplay of cellular signals and processes.[13] When cells experience DNA damage, they activate a variety of signalling pathways that trigger the process of apoptosis.[13,14,15] One of these pathways includes the activation of enzymes known as caspases, which cleave and destroy key cellular components, leading to the death of the cell.[13,14,16] This is the activation of caspase-independent apoptosis.[13] Specifically, it triggers caspases through the p53 protein when DNA is damaged in mammalian cells. The DNA damage signalling network causes the stabilization and activation of p53[17], which boosts the transcription of pro-apoptotic genes, such as Puma[15,18] and Noxa[15]. These genes produce BH3-only proteins[13] that inactive anti-apoptotic Bcl2-family proteins[13] and activate Bax or Bak[13], resulting in the release of cytochrome C from the mitochondria[19]. The cytochrome C then binds to Apaf-

1, leading to the formation of the apoptosome, which activates caspases and initiates apoptosis[20] (shown in **Figure 2.2**).

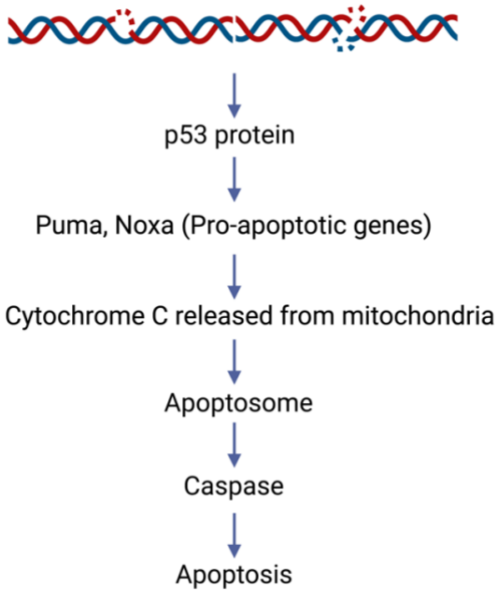

Figure 2.2 Mechanism of activation of caspase-dependent apoptosis by DNA damage.

2.2.2 Caspase-3 Inhibitor (Peptide Z-DEVD-FMK)

In our experimental studies, we aimed to not only examine the metabolic profiles of radiation-resistant cells at different time points post-therapy but also to determine the origin of these metabolites. Specifically, we wanted to determine if the metabolic profiles we collected were produced by alive or apoptotic cells.

In order to achieve this goal, we used a Caspase-3 inhibitor (Peptide Z-DEVD-FMK) to inhibit the MCF-7 cell apoptosis after the cells got irradiated. Caspases are a family of cysteine proteases that play a key role in the process of apoptosis or programmed cell death.

Caspase-3 inhibitor (Peptide Z-DEVD-FMK) is a peptide that acts as an inhibitor of the caspase-3 enzyme.[21] The caspase-3 inhibitor Peptide Z-DEVD-FMK works by binding to the active site of caspase-3, blocking its enzymatic activity.[22] This effectively prevents caspase-3 from cleaving its target substrates, which are proteins that are involved in the regulation of apoptosis.[22] By blocking caspase-3 activity, Peptide Z-DEVD-FMK can inhibit apoptosis and preserve cell survival. This method ensures the improvement of cell viability after ionizing radiation, allowing the determination of whether the collected metabolic markers are from live cells.

2.2.3 Intensity of Radiation Therapy

One important aspect of radiation therapy is the dose intensity, which refers to the amount of radiation delivered to the patient. The goal of radiation therapy is to deliver enough radiation to destroy cancer cells while minimizing damage to healthy tissues. Hence, radiation is typically delivered in smaller doses over a longer period. This is known as fractionated radiotherapy.[23]

The dose in radiation therapy is determined by several factors, including the type of cancer being treated, the location of the cancer in the body, and the patient's overall health. The radiation oncologist, who is the doctor responsible for designing and overseeing the radiation therapy plan, takes all of these factors into consideration when determining the appropriate dose intensity.[24] In general, the dose intensity of radiation therapy is expressed in units of gray (Gy).[25] One gray is equivalent to the absorption of one joule of radiation energy per kilogram of tissue.[25] The total dose of radiation delivered during a course of radiotherapy is typically between 45-60 Gy,[26] with smaller doses given each day over a period of several weeks. In our experimental studies, two different doses of ionizing radiation: 5 Gy (weak) and 20 Gy (strong) were chosen to expose on the MCF-

7 breast cancer cell line. These doses were chosen to examine the effects of varying levels of radiation on breast cancer cells.

2.3 Raman Scattering

Raman scattering is named after its discoverer, the Indian physicist C. V. Raman[27], who first observed the effect in 1928. Raman was working on understanding the scattering of light in liquids and noticed that a small fraction of the scattered light had a different frequency (inelastic scattering) than the incident light. He attributed this shift in frequency to the scattering of light by the molecules in the liquid, which caused the molecules to vibrate and emit scattered light at slightly different frequencies. This discovery opened a new field of study in spectroscopy, known as Raman spectroscopy, which has become a powerful tool for studying the vibrational and rotational properties of molecules in a wide range of fields, from chemistry and physics to materials science and biology.

Jablonski diagrams (shown in **Error! Reference source not found.**) are energy-level diagrams that illustrate the various quantum states and possible transitions in molecules. They can be used to explain the principles of Rayleigh scattering, Stokes scattering, and anti-Stokes scattering.

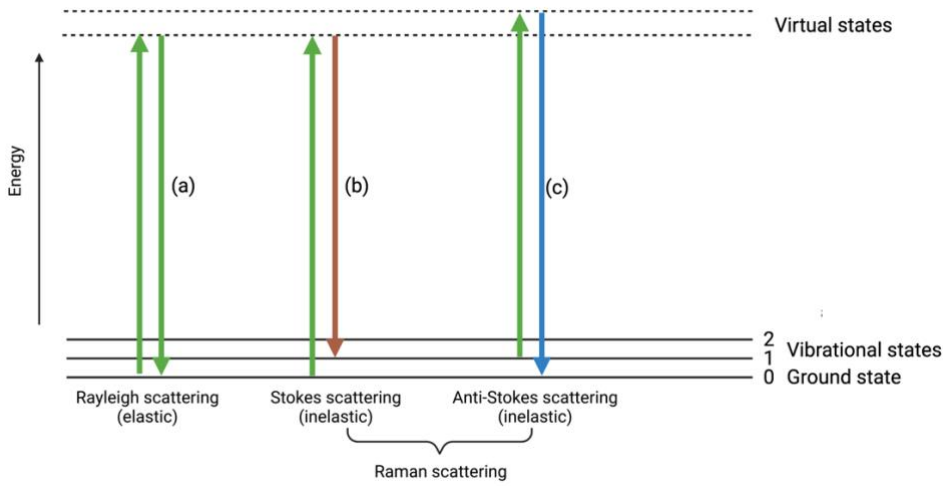

Figure 2.3. Schematic Jablonski diagrams illustrating the processes of Rayleigh and Raman scattering.

Rayleigh scattering is the dominant process in the majority of scattering events. In this case, the energy of the molecule is unchanged after interaction with the photon. On a Jablonski diagram, Rayleigh scattering (Error! Reference source not found.**a**) is represented as the molecule being excited to any virtual state and relaxing back to its original state so that the scattered photon has the same energy as the incident photon. In Stokes scattering (Error! Reference source not found.**b**), the incident photon takes the molecule to an excited virtual state. Then the molecule relaxes back to a higher vibrational state than it had originally, emitting a photon with lower energy than the incident photon. The energy difference between the initial and final states is a vibrational quantum that is further released as heat once the molecule relaxes to the ground vibrational state. In anti-Stokes scattering (Error! Reference source not found.**c**), the molecule begins in a vibrationally excited state and is excited to any virtual state. However, the molecule relaxes back to a lower vibrational state than it had originally and the scattered photon leaves with higher energy than the excitation photon.

From a quantum mechanical perspective, Stokes and anti-Stokes transitions are equally likely processes. However, in fact, anti-Stokes scattering is less frequent than Stokes because it requires the molecule to be in a vibrationally excited state before the photon interacts with it. The anti-Stokes signal is then weaker in intensity, and it is often filtered. As a result, Raman measurements usually rely only on Stokes scattering. The relative intensities of Rayleigh, Stokes and anti-Stokes scattering can be seen in **Figure 2.4**. The energy difference between the incident and scattered light (vibrational frequency) is called "Raman shift" and it is typically presented in wavenumber (cm^{-1}) in a Raman spectrum.

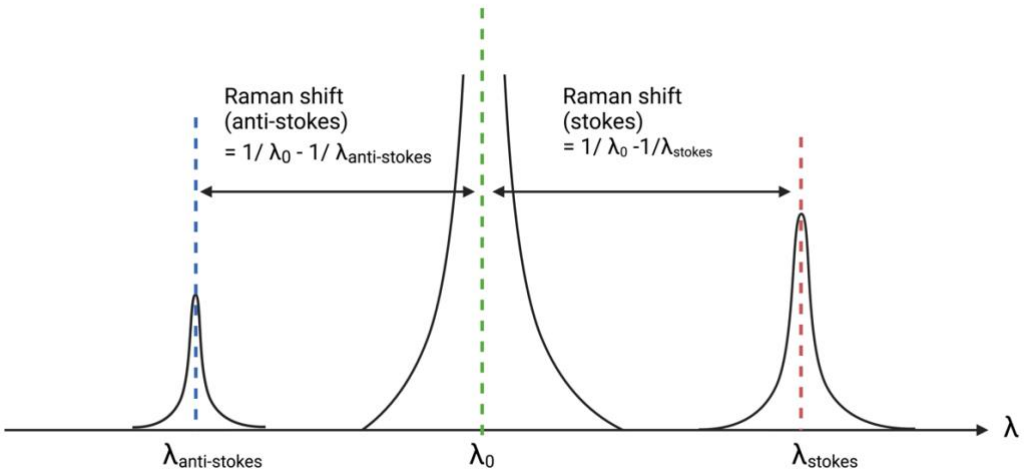

Figure 2.4. The relative intensity of the Stokes and anti-Stokes scattering relative to Rayleigh scattering.

2.4 Classical Raman Theory

The classical theory of electromagnetic radiation posits that oscillating electric and magnetic fields at a particular frequency can give out electromagnetic radiation of the same frequency. This theory can be applied to explain light scattering phenomena. For most

systems, only an induced electric dipole moment μ is taken into consideration. This dipole moment which is induced by the electric field **E** could be expressed by the power series:

$$\mu=\mu^{(1)}+\mu^{(2)}+\mu^{(3)}+\cdots \qquad (\textit{Equation 1})$$

where

$$\mu^{(1)}=\alpha\cdot\mathbf{E} \qquad (\textit{Equation 2})$$

$$\mu^{(2)}=\frac{1}{2}\beta\cdot\mathbf{EE}$$

$$\mu^{(3)}=\frac{1}{6}\gamma\cdot\mathbf{EEE}$$

The polarizability tensor, denoted by α, is a second-order tensor whose components are measured in the unit of $CV^{-1}m^2$. The orders of magnitude for the components α, β and γ are $10^{-40}\ CV^{-1}m^2$, $10^{-50}\ CV^{-2}m^3$ and $10^{-61}\ CV^{-3}m^4$. Based on these values, the contributions of $\mu^{(2)}$ and $\mu^{(3)}$ are negligible unless the electric field is extremely high. As Rayleigh and Raman scattering can be observed at much lower electric field intensities, it is reasonable to explain these phenomena in terms of $\mu^{(1)}$ only.

Next, how a molecular system interacts with a harmonically oscillating electric field at the frequency ω_0 will be considered. The vibrational part will be considered while the rotation will be ignored. Since the polarizability of the system is anticipated to vary with the nuclear coordinates, we can express the changes in the components of the polarizability tensor with respect to the vibrational coordinates using a Taylor series.

$$\alpha_{ij}=(\alpha_{ij})_0+\sum_k\left(\frac{\partial\alpha_{ij}}{\partial Q_k}\right)_0 Q_k+\frac{1}{2}\sum_{k,1}\left(\frac{\partial^2\alpha_{ij}}{\partial Q_k\,\partial Q_l}\right)_0 Q_kQ_l+\cdots \qquad (\textit{Equation 3})$$

where $(\alpha_{ij})_0$ is the α_{ij} value at the equilibrium configuration, Q_k and Q_l are normal coordinates of vibration at frequencies ω_k, ω_l. To simplify the calculations, we will assume a harmonic approximation and disregard terms which involve powers of Q higher than the first. After initially fixing our attention on one normal mode, Q_k, we could get

$$\alpha_{ij} = (\alpha_{ij})_0 + \left(\frac{\partial \alpha_{ij}}{\partial Q_k}\right)_0 Q_k \qquad (\textit{Equation 4})$$

Since for a harmonic vibration:

$$Q_k = Q_{k0} \cos(\omega_k t + \delta_k) \qquad (\textit{Equation 5})$$

We could get the expression of α tensor resulting from k-th vibration:

$$\alpha_{ij} = (\alpha_{ij})_0 + \left(\frac{\partial \alpha_{ij}}{\partial Q_k}\right)_0 Q_{k0} \cos(\omega_k t + \delta_k) \qquad (\textit{Equation 6})$$

Therefore, according to *Equation 2*, under the influence of electromagnetic radiation at frequency ω_0, the induced electric dipole moment $\mu^{(1)}$ is expressed:

$$\mu^{(1)} = \alpha_k \cdot E_0 \cos\omega_0 t = \alpha_0 \cdot E_0 \cos\omega_0 t + \left(\frac{\partial \alpha_k}{\partial Q_k}\right)_0 \cdot E_0 Q_{k0} \cos\omega_0 t \cos(\omega_k t + \delta_k) t =$$

$$\alpha_0 \cdot E_0 \cos\omega_0 t + \frac{1}{2}\left(\frac{\partial \alpha_k}{\partial Q_k}\right)_0 \cdot E_0 Q_{k0} \cos(\omega_0 t + \omega_k t + \delta_k) + \frac{1}{2}\left(\frac{\partial \alpha_k}{\partial Q_k}\right)_0 \cdot E_0 Q_{k0} \cos(\omega_0 t - \omega_k t - \delta_k)$$

(*Equation 7*)

We can see that the linear induced dipole moment $\mu^{(1)}$ is comprised of three components with different frequencies. $\alpha_0 \cdot E_0 \cos\omega_0 t$ gives rise to radiation at ω_0 and accounts for the Rayleigh scattering. $\frac{1}{2}\left(\frac{\partial \alpha_k}{\partial Q_k}\right)_0 \cdot E_0 Q_{k0} \cos(\omega_0 t + \omega_k t + \delta_k)$ gives rise to radiation at $\omega_0 + \omega_k$ and accounts for the anti-Stokes Raman scattering. $\frac{1}{2}\left(\frac{\partial \alpha_k}{\partial Q_k}\right)_0 \cdot E_0 Q_{k0}$

$\cos(\omega_0 t - \omega_k t - \delta_k)$ gives rise to radiation at ω_0-ω_k and accounts for the Stokes Raman scattering.

These mathematical manipulations provide a helpful qualitative description of the mechanisms behind Rayleigh and Raman scattering within the context of classical radiation theory. Rayleigh scattering results from the dipole of the molecule oscillating at frequency ω_0 due to the electric field of the incident radiation. On the other hand, Raman scattering arises due to the dipole moment oscillating at frequencies $\omega_0 \pm \omega_k$, which is produced by the interaction between the dipole oscillation at ω_0 and the molecular vibration at frequency ω_k. In other words, the frequencies observed in Raman scattering represent beat frequencies of the radiation frequency ω_0 and the molecular vibrational frequency ω_k.

2.5 Surface-enhanced Raman Scattering

Surface-enhanced Raman scattering (SERS) was first observed in the mid 1970s, when Fleischmann et al. reported a dramatic enhancement of the Raman scattering signal from pyridine molecules adsorbed on roughened silver electrodes.[28] It is widely acknowledged that the enhancement is primarily driven by two main processes: the electromagnetic and the chemical mechanism.

2.5.1 The Electromagnetic (EM) Mechanism

Electromagnetic (EM) enhancement arises from the interaction between the incident light and the free-electrons present in the substrates (e.g., metallic nanoparticles) used in SERS. When metallic nanoparticles are irradiated by an incident light that resonantly matches the frequency from the collective oscillations of conduction band electrons, a highly localized and enhanced electromagnetic field is produced in the vicinity of the nanoparticles. This phenomenon is known as localized surface plasmon resonance (LSPR). The location of the plasmon resonance (ω_p) is a function of the free carrier density

(N) of the substrate, with m^* representing the effective mass of the charge carriers (electrons or holes)[29]:

$$\omega_p = \left(\frac{4\pi Ne^2}{\varepsilon_\infty m^*}\right)^{1/2} \qquad \text{(Equation 8)}$$

Metals such as Ag, Au, and Cu have the highest free carrier densities (ranging from 10^{-22} to 10^{-23} cm^{-3}), which makes them accessible to plasmon resonance in the visible region. As a result, they are frequently used as plasmonic substrates for SERS.

Schlücker[30] has described how the fundamental physics of the driven harmonic oscillator can qualitatively explain the concept of the LSPR-magnified field. In summary, when resonant elastic light scatters off a metallic sphere, an increased local field E_{loc} relative to the incident field E_0 is generated at the metal surface. This enhanced electromagnetic field is the basis of EM-based SERS in plasmonic substrates, where both incident laser and Raman scattering light are electromagnetically enhanced in two successive steps. The first step involves local field enhancement near the plasmonic nanoparticles at the resonant incident frequency (ω_0), while the second step involves the further enhancement of Raman scattered light when the Raman frequency (ω_R) overlaps with the plasmon resonance. Since the frequencies of the incident laser light and Stokes Raman scattering in the probe molecule are similar ($\omega_0 \approx \omega_R$), the signal intensity enhancement (I_M) is roughly proportional to the fourth power of the local field amplitude (E_{loc} / E_0), as described by the equation below:

$$I_{\mathrm{M}} = \frac{|E_{\mathrm{loc}}\omega_0|^2|E_{\mathrm{loc}}\omega_{\mathrm{R}}|^2}{|E_0\omega_0|^2|E_0\omega_{\mathrm{R}}|^2} \approx \frac{|E_{\mathrm{loc}}\omega_{\mathrm{R}}|^4}{|E_0\omega_0|^4} \qquad \text{(Equation 9)}$$

It is worth mentioning that the degree of enhancement is not influenced by the characteristics of the analyte molecules. Instead, it is dictated by the intensity of the

electromagnetic fields when plasmonic metals are present. These fields can be adjusted by manipulating factors such as the morphology of nano-structures, dielectric functions, and interparticle plasmonic coupling. By doing so, it is possible to create electromagnetic hot spots between adjacent metal particles.

2.5.2 The Chemical Mechanism

The chemical mechanism (CHEM) involves the intrinsic features of the adsorbate and the new properties arising when the adsorbate is combined with the substrate (adsorbate–metal complex) under the effect of the incident light. It is not compulsory for the substrate to be plasmonic, rough or nanostructured for the CHEM to occur.[31] So far, the primarily recognized contribution to the CHEM mechanism arises from the charge transfer (CT) between the metal and the molecule of interest. When the molecule is chemisorbed to the surface, the incident light is able to excite an electron from the highest occupied molecular orbital (HOMO) into lowest unoccupied molecular orbital (LUMO) through indirect coupling with the metal (Shown in **Figure 2.5**). Alternatively, the incident light may be in resonant with the molecule-metal complex and can directly excite an electron from the HOMO into an unoccupied orbital.

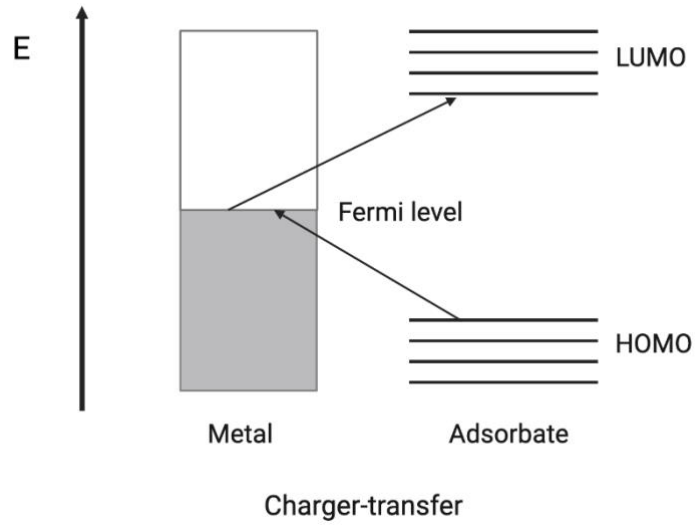

Figure 2.5. Schematic of chemical mechanisms (charge transfer) for SERS enhancement. The charge transfer involves indirect excitation through the metal.

2.6 Coffee-ring Effect-based Substrate

The coffee-ring effect is a well-known phenomenon in which the deposition of particles from a drying liquid forms a ring-like pattern on a solid surface. The effect is named after the characteristic ring-like stain that is left behind when a drop of coffee dries on a flat surface, but it can be observed with many other liquids and particles. In the context of SERS, the coffee ring effect can be used to create substrates with enhanced Raman signals.[32] In the context of SERS, the concentration of both analyte molecules and nanoparticles increase at the edges of a droplet due to the coffee ring effect, which leads to an enhancement of the Raman signals.

The coffee ring effect is caused by a combination of capillary flow, evaporation, and surface tension.[33,34] When a droplet of a solution containing both solvent and solute is placed on a flat surface, the solvent begins to evaporate, and the rate of evaporation is highest at the edges of the droplet. The evaporation process induces a capillary flow within

the droplet which drives the suspended particles toward the edges, leaving a ring-shaped structure (**Figure 2.6**). The suspended particles are carried along with the flow of solvent, but they are not carried away by the evaporation of the solvent, so they tend to get left behind and accumulate at the edges of the droplet. This creates a ring-like pattern of solute particles on the surface, which is known as the coffee ring effect.

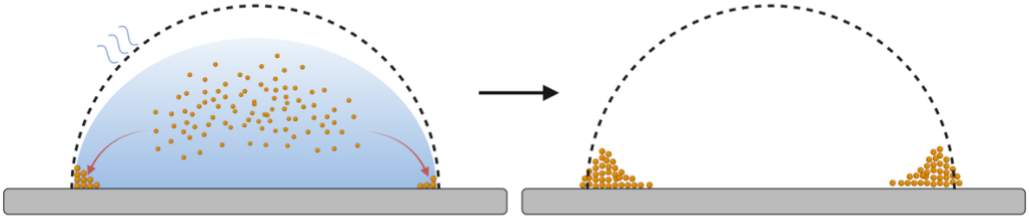

Figure 2.6. Capillary outflows transport the silver nanoparticles to the drop edge forming ring stains.

The coffee ring effect is influenced by several factors, including the viscosity of the solvent, the size and shape of the droplet, and the size and concentration of the solute particles.[34] These factors determine the rate at which the solvent evaporates and the rate at which the solute particles are carried along with the flow of solvent, which ultimately determine the final concentration profile of the solute particles on the surface.

2.7 Principal Component Analysis (PCA)

Principal Component Analysis (PCA) is a statistical technique used to analyze large data sets by identifying patterns and relationships between variables. In essence, PCA transforms a high-dimensional data set into a lower-dimensional one by identifying the most important patterns or features in the data and representing them as linear combinations

of the original variables. While PCA allows for the visualization of datasets by reducing them into two or three dimensions, it comes with the drawback of information loss during the process since the lower-dimensional representation may not capture all the subtle details present in the original data.

PCA can be used in SERS to help identify the important features and reduce the noise in the data. For instance, when collecting numerous SERS spectra of various samples, PCA can help to reduce the dimensionality of the data by identifying the most significant spectral features that differentiate the samples. This can help in identifying common spectral features that are associated with a specific sample or chemical group, which can be used for either identification or classification purposes. In our experiments, hundreds of SERS spectra from the cell culture supernatant were collected at different time points after ionizing radiation and then analyzed by PCA. A statistical program code in MATLAB® carries out the PCA. Before combining all the spectra from different groups into one dataset, the spectra should be pre-processed to remove noise and baseline fluctuations and should be normalized to account for differences in signal intensity. Then PCA is performed on the standardized dataset to extract the principal components. The first principal component is the component that captures the largest amount of variance, and the second principal component is the component that captures the second-largest amount of variance. The percentage associated with each principal component indicates the proportion of the total variance in the data due to each component. The contribution of each principal component to the total variance can help identify features or variables that are most important for the interpretation of the data.

Chapter 3. Experiment Details

3.1 MCF-7 Cell Culture

Pre-frozen MCF-7 cell pellets stored in liquid nitrogen were planned for thawing and plating as required to perform radiotherapy. The vials of MCF-7 cell pellet were removed from the liquid nitrogen storage and transferred to a water bath for thawing at 37 °C for 2 min. They were removed from the water bath just before complete thawing. Following that, the cells were gently resuspended and transferred to a 15 mL sterile conical tube containing 9 mL pre-warm, 37 °C, cell culture medium (Dulbecco's modified Eagle's medium containing 10% (v/v) fetal bovine serum). Subsequently, the cells were centrifuged to a cell pellet at 200× g for 5 min, the supernatant was removed and the pellet resuspended in 1-2 mL of pre-warmed cell culture medium. The cells were plated in the cell culture vessel (T-25 cell culture flask, surface area: 25 cm^2) and allowed to grow for 3 days until the medium changed.

MCF-7 cell was passaged when cell confluency reached 80-90%. Firstly, the cells need to be detached from the flask's inner surface with trypsinization. All spent medium from the cell culture vessel was aspirated from the flask followed by gently rinsing the surface of the cell layer once with 1× phosphate-buffered saline (PBS). Next, 2 mL diluted 0.25% trypsin-EDTA solution (unlock passaging reagent) was added into the vessel and distributed over the entire cell layer. The cells were detached from the flask surface and were observed under the microscope after incubation for 5-10 min at 37 °C. Thereafter, the trypsin was neutralized with an equal volume of pre-warm culture medium to make sure that cell viability was maintained. Following that, the cell suspension was transferred to a centrifuge tube and centrifuged at 300× g for 5 minutes. The supernatant was then removed,

and the cell pellet was resuspended in a fresh culture medium to create a single-cell suspension. Eventually, the cells were plated in a new culture vessel (T-75 cell culture flask, surface area: 75 cm^2) at 1×10^6 cells/flask seeding density and covered with enough pre-warm culture medium to conduct the subculture. The new generation of cells was incubated at 37 °C, 5% CO_2 in a humidified incubator.

3.2 Collection of Samples from the Supernatant of Irradiated Cells

In order to undergo radiation therapy at the BC Cancer Agency, live MCF-7 cells must be transported within several hours. The cells were first detached from the flasks, where they had reached 100% confluency, and transferred to 15 mL Falcon tubes, which were sealed for transport. Once at the facility, the cells were exposed to 5 Gy and 20 Gy doses and then brought back to the Biocore Facility for further processing. The irradiated cells were then centrifuged to remove any immediate dead cells, leaving only the cells that survived the radiation. These surviving cells were cultured in 12-well plates at a specific seeding density, allowing for the collection of the supernatant samples containing the metabolic markers released from resistant cells in separate wells at different time points following the radiation therapy.

3.2.1 Cells Counting

A counting chamber was used to count the number of cells and assure that the same amount of cells is plated in each well. The counting chamber is a type of slide used to determine the number of cells per unit volume of a suspension. The most widely used type of chamber is called a hemocytometer because it was originally designed to perform blood cell counts.

The hemocytometer must be appropriately prepared before applying the fluid containing cells to ensure accurate cell counting. Proper mixing was necessary to achieve a homogenous suspension, as clumped cells were difficult to count and not evenly distributed. The concentration of the cells should also be appropriate; a concentration that was too high leads to overlapping cells, while a concentration that was too low results in a higher statistical error and requires more time to count. Our irradiated MCF-7 cell suspension was diluted in 1:10 proportions. To create a 1:10 dilution, 1 part of the sample was mixed with 9 parts of fresh culture medium, and the dilution should be considered when calculating the final concentration.

The counting chamber was prepared by first cleaning the polished surface with lens paper, ensuring that it was free of any debris or smudges. The coverslip, which is thicker than those used in conventional microscopy to overcome the surface tension of liquid drops, was also carefully cleaned. Once both surfaces were prepared, the coverslip was placed onto the counting surface, ready to receive the cell suspension. A small volume of 10 μl prepared cell suspension was then pipetted into one of the V-shaped windows of the counting chamber (shown in **Figure 3.1**) using a micropipette. The liquid filled the space under the coverslip by capillary action, and enough was added to ensure that the mirrored surface was just covered. Finally, the charged counting chamber was placed onto the microscope stage and the counting grid was brought into focus.

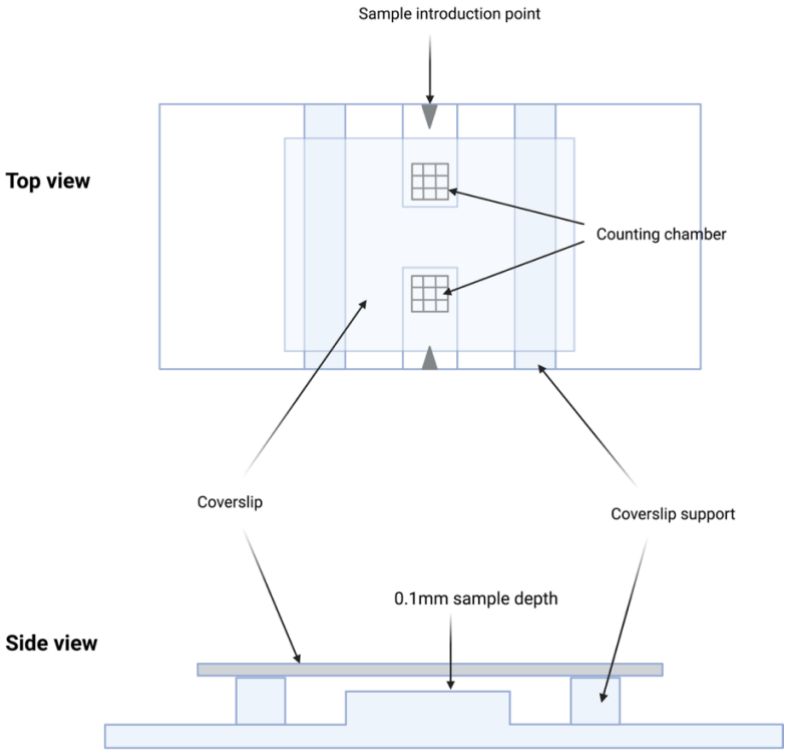

Figure 3.1. Schematic views of a hemocytometer.

The grid is etched into the glass, composed of squares of various sizes that facilitate cell counting. By utilizing this method, the number of cells present in a given volume can be calculated accurately. The grid is divided into 9 large squares (A, B, C, and D squares are the four corners), arranged like a tic-tac-toe grid (shown in **Figure 3.2 left**). Each of these large squares occupies an area of 1 mm^2, and the chamber has a depth of 0.1 mm (shown in **Figure 3.2 right**). Therefore, the entire counting grid is situated within a volume of 0.9 mm^3.

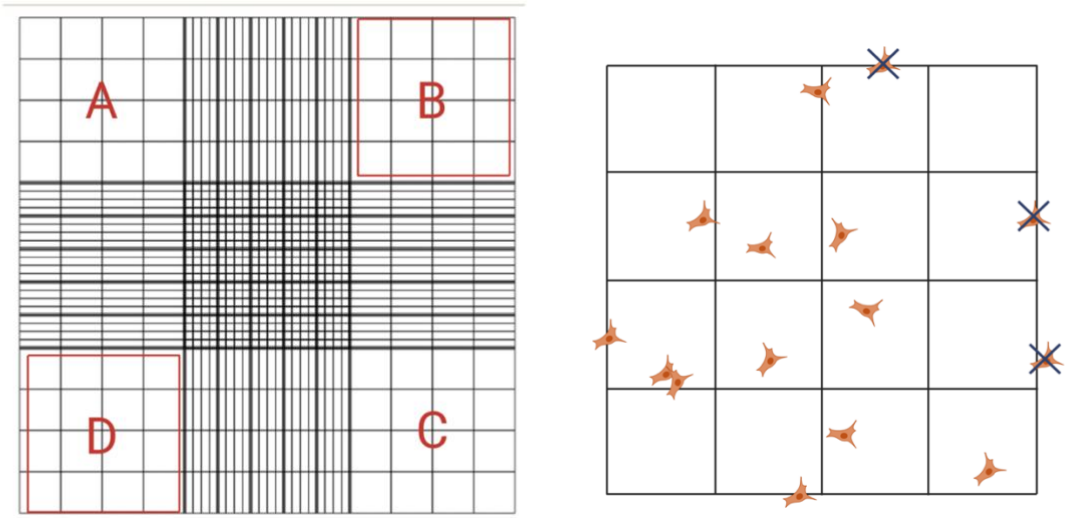

Figure 3.2. The grid layout of the hemocytometer (left) and the cell counting rules in one large square (right).

There are some basic rules when we count the cells. For MCF-7 cells, which are large cells, the four large corner squares and the middle one needed to be counted. However, cells that intersect with the grid lines require careful consideration. Cells that contacted the top or right line of a square should not be included in the count, while cells that overlapped the bottom or left line of a square should be included. For example, in **Figure 3.2 right**, the top and right three cells on the grid will exclude from the count while the bottom and left two cells will be included in the cell counting.

For example, if there were 125 cells in the five large squares of the counting chamber, which represents a volume of 0.5 mm^3. In this case, the cell density can be calculated as 250 cells per mm^3, which is equivalent to 250,000 cells per ml. Since the original cell suspension had been diluted by 10 times, the original cell suspension density should be 2.5×10^6 cells per ml.

3.2.2 Cells Plated in Well Plate

With the exception of the supernatant of the cell collected one day after radiation therapy, all other samples were acquired at three-day intervals. This is because the cell culture medium was changed every three days. The irradiated cells were seeded in a 12-well plate at a density of 1.5×10^4 cells per ml, with two rows dedicated to the 5 Gy and 20 Gy irradiated cells, respectively. An additional row was dedicated to the control group (0 Gy dose) (shown in **Figure 3.3**). Each well contained 1 ml of culture medium. In conclusion, we collected the supernatant containing metabolic markers released from the resistant cells at 1, 4, 8, and 12 days after radiotherapy.

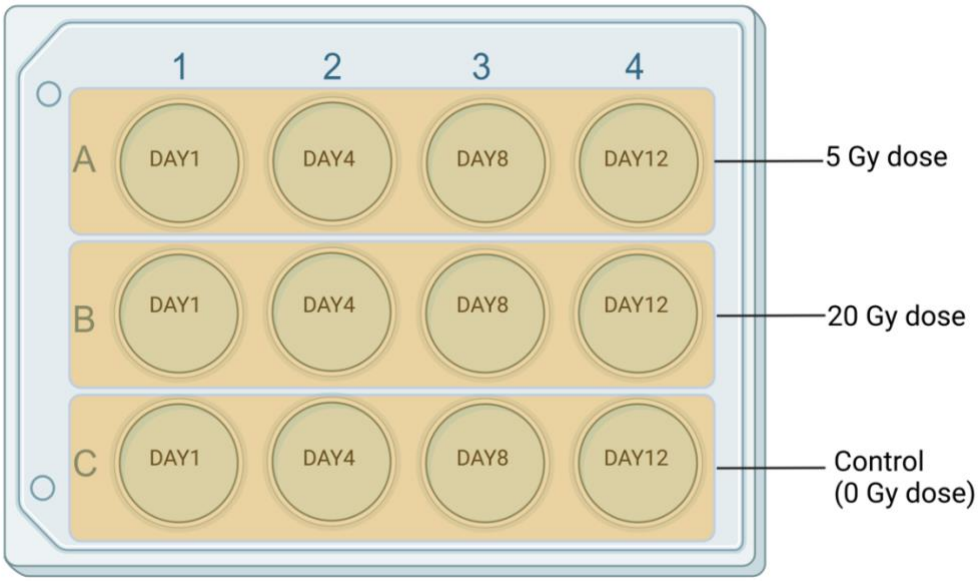

Figure 3.3. Control and two doses of irradiated cell metabolism samples were collected on day 1, day 4, day 8, and day 12.

3.3 SERS Substrate Fabrication

3.3.1 Silver Nanoparticles Synthesis

Silver nitrate ($AgNO_3$, MW = 169.88 g/mol), and sodium citrate dihydrate ($C_6H_5Na_3O_7 \cdot 2H_2O$, MW = 294.10 g/mol) were purchased from Sigma. All chemicals were used without further purification. Ultrapure water acquired from a Milli-Q Nanopore System was used in the preparation of silver nanoparticles. The glassware used in the synthesis was cleaned and rinsed thoroughly with ultrapure water.

UV-Vis spectrum was recorded on Perkin Elmer Lambda 1050 UV-Vis-NIR spectrometers using standard quartz cells at room temperature. Transmission electron microscopy (TEM) image was taken with a JEOL 1011 transmission electron microscope. The TEM specimen preparation: All TEM grids were prepared from the freshly prepared Ag NPs suspension. 5 μl of the solution was added to each grid. The grids clamped by tweezers were placed under a glass dish to allow for slow drying (1–2 h) of the silver nanoparticles (AgNPs) suspension.

The Lee-Meisel method[35] (**Figure 3.4**) was employed to synthesize citrate-coated spherical AgNPs. 0.045g $AgNO_3$ was dissolved in 250 ml of distilled water and heated to boiling. Thereafter, 10 ml of an aqueous solution containing 0.05 g sodium citrate dihydrate was added dropwise under vigorous stirring. The solution was kept boiling for at least 1 hour. The normalized UV–Vis spectrum of the citrate-coated AgNPs exhibits an absorption brand at 416 nm due to plasmon resonance (**Figure 3.6**). **Figure 3.5** shows that the citrate-coated AgNPs were found to have diameters in the range of 30 to 50 nm with a nearly spherical shape. The existence of a single surface plasmon resonance peak at 416 nm in the UV–Vis spectrum and the TEM image indicates the successful synthesis of the citrate-coated spherical AgNPs. It is worth mentioning that the UV-Vis spectrum of the citrate-

coated AgNP colloidal solution remained unchanged over several months, indicating that the citrate-coated AgNPs became very stable in time.

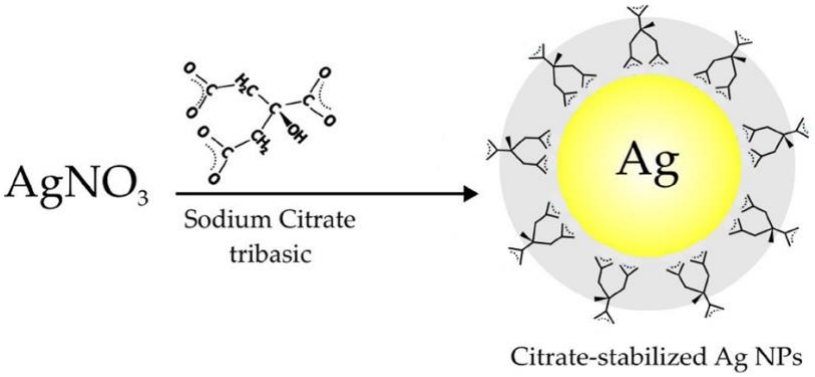

Figure 3.4. Schematic of the synthesis of sodium citrate-coated spherical silver nanoparticles

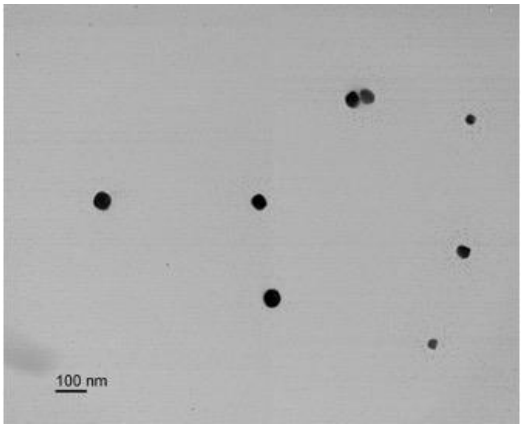

Figure 3.5. TEM image of sodium citrate-coated silver NPs.

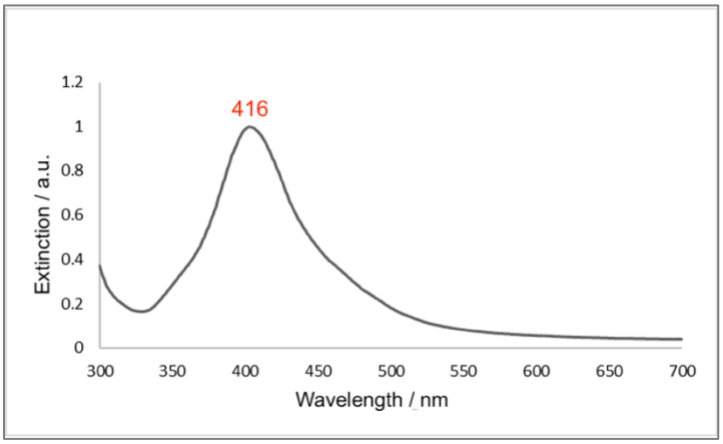

Figure 3.6. Normalized UV-Vis spectrum of citrate-coated silver NPs.

3.3.2 Coffee-ring Effect-based Substrate Fabrication

Our coffee-ring effect-based Ag nanoparticles substrate was fabricated by spiking 10 μl of prepared Ag nanoparticles suspension on a cleaned (by piranha solution and ethanol) microscope glass slide (22 × 22 mm) and drying for 1 hour at room temperature in the air. During the drying process, the coffee-ring effect (discussed in **Section 2.6**) came into play, resulting in the formation of ordered rings of Ag nanoparticles on a glass slide (shown in **Figure 3.7**).

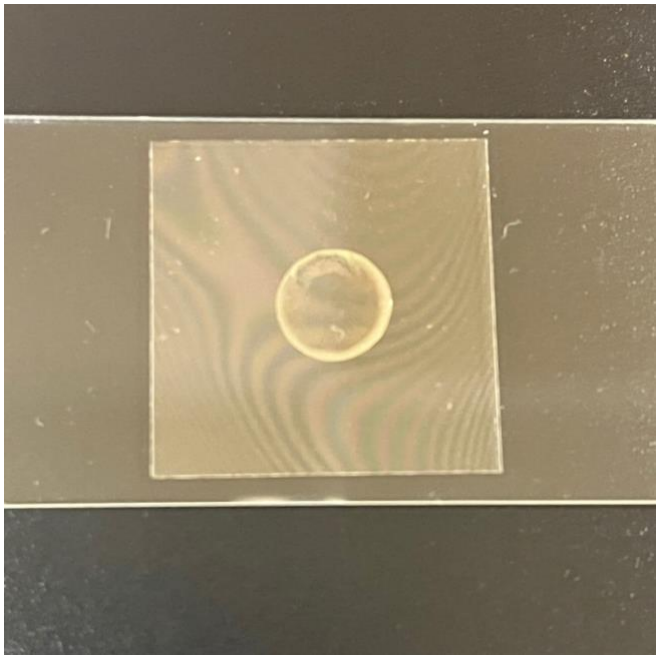

Figure 3.7. Image of coffee ring-based Ag nanoparticle substrate.

3.4 SERS Experiment

10 μl of the collected supernatant of the cell cultures containing metabolites were pipetted on the AgNPs ring in the SERS substrate and left to dry in the air at room temperature for one hour. SERS spectra were collected after drying.

The Renishaw inVia Raman spectrometer (schematic view shown in **Figure 3.8**) uses a 785-nm laser source and was employed to record the SERS spectra (ranging from 300 cm^{-1} to 1400 cm^{-1}) using the Raman mapping acquisition mode. 25 spectra were mapped in six different squares (5×5×6 to a total of 150 spectra) across various locations on the silver nanoparticles ring. This approach prevents significantly large spatial variations from impacting the mean spectrum of each sample. The setup for the Raman system involves a microscope for both sample illumination and capturing of the resulting scattered light. A long-working-distance objective lens with a 50x magnification and 0.55 numerical aperture was used focus the laser beam on the silver nanoparticles ring in the substrate. The microscope system gathers the light scattered from the cell via the same objective employed for excitation. A filtering process is then utilized to extract the small fraction of light that underwent Raman scattering. The Raman scattered light is subsequently split into its constituent wavelengths utilizing a diffraction grating, and the spectrum produced is detected with a CCD camera.

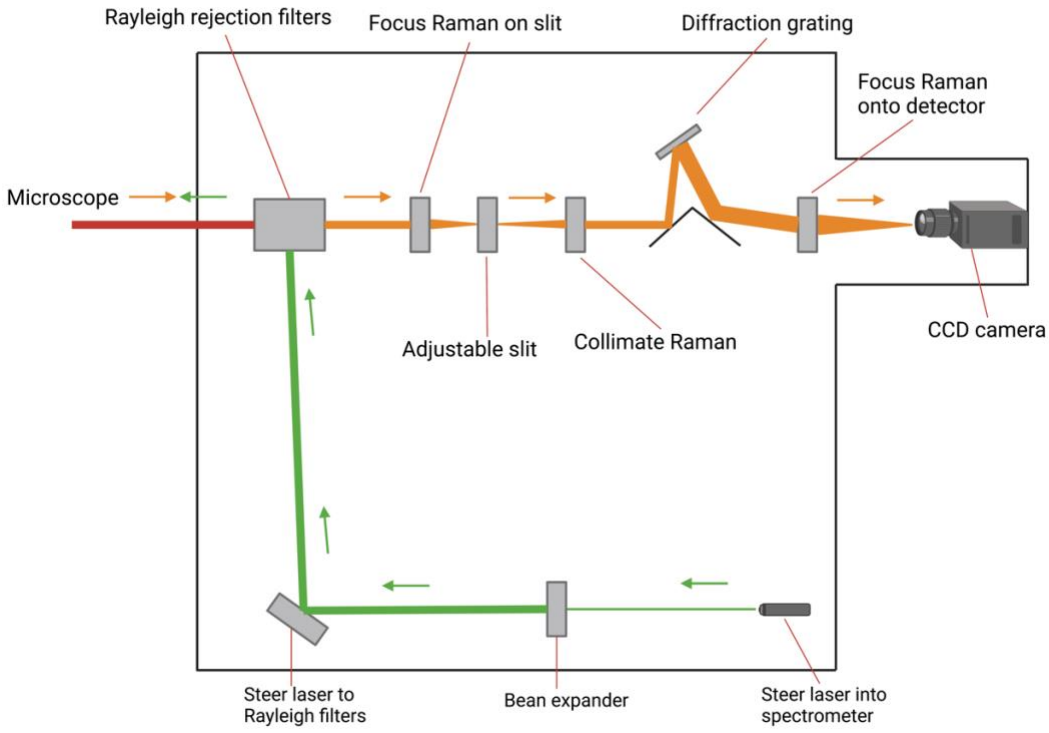

Figure 3.8. Schematic view of the Renishaw inVia Raman microscope system.

3.5 Caspase-3 Inhibitor Treatment

As shown in Chapter 2.22, the caspase-3 Z-DEVD-FMK Inhibitor was used to treat the MCF-7 cells to improve cell viability. Caspase-3 Z-DEVD-FMK Inhibitor must be reconstituted using highly pure DMSO. Upon reconstitution in DMSO, the stock solution should be stored at -20 °C. To prepare the stock solution, 1.5 ml of DMSO was added to the 5 mg inhibitor to yield a 5 mM stock solution and aliquoted to avoid multiple freeze and thaw cycles.

The resistant cells were subjected to treatment with a 50 μM of Caspase-3 Z-DEVD-FMK inhibitor. After administering two doses of ionizing radiation (5 Gy and 20 Gy) to MCF-7 cells, the resistant MCF-7 cells were centrifuged to form a pellet and suspended in a fresh culture medium to eliminate the dead cells. The cell suspension was

then diluted to a concentration of 1.5×10^5 cells per ml and dispensed into two 12-well plates, with 1 ml of diluted cell suspension added to each well. Group A and group B were designated to receive culture medium with and without Z-DEVD-FMK caspase inhibitor, respectively (shown in **Figure 3.9**). Before use, the culture medium with or without the Caspase-3 inhibitor needed to be warmed to 37 °C using a water bath.

For Group A, the culture medium with Z-DEVD-FMK caspase inhibitor was prepared by diluting 150 µl of the thawed stock inhibitor solution with 15 ml of culture medium, resulting in a final inhibitor concentration of 50 µM. For Group B, a culture medium with DMSO was prepared by diluting 150 µl of DMSO with 15 ml of culture medium.

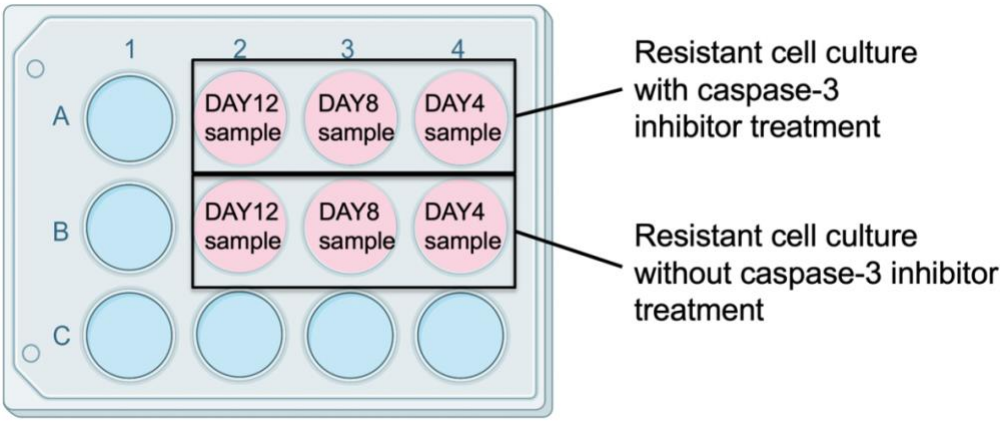

Figure 3.9. Resistant cell culture with and without caspase-3 inhibitor treatment in a well plate.

After a 24-hour pre-incubation period to allow cell attachment, the culture medium was replaced with the respective prepared medium for each group. On day 4, 8, and 12, supernatant samples were collected from one well of each group for additional SERS measurement. During this time, the medium in the remaining wells of both groups was replaced with corresponding fresh pre-warmed medium to sustain the resistant cells.

3.5.1 Cell Viability Test

To determine the percentage of viable cells in cell suspensions after caspase inhibitor treatment, the Trypan Blue Exclusion Assay was performed. The assay utilized Trypan Blue dye (Sigma-Aldrich T8154) which selectively stains non-viable cells with damaged cellular membranes. The living cells with intact membranes appear transparent, while the dead or dying cells that have taken up the dye appear blue under the microscope.

A homogenous mixture of 90 μL of cell suspension and 10 μL of 0.4% trypan blue dye was prepared and pipetted into the counting chamber. The percentage of viable and non-viable cells was quantified under the optical microscope. This process was repeated three times, and a t-test was conducted to compare the cell viability between the caspase inhibitor treatment group and the control group.

Chapter 4. Result and Discussion

This chapter will present the results of the SERS analysis of various supernatant samples from irradiated MCF-7 cancer cells. The spectra were preprocessed using the language of MATLAB to adjust the baseline and normalize the intensities. Principal component analysis (PCA) was employed to compare the SERS spectra of the irradiated and control groups. Furthermore, the identification of the potential biomarkers (Hypoxanthine) in cell metabolism and the investigation of the origin of this potential biomarker will be included in this chapter.

4.1 SERS Results of Supernatant Samples from 0, 5, 20 Gy Irradiated Cells

4.1.1 SERS Results on Day 1

To account for the presence of the spent culture medium in the supernatant samples, we collected the Raman spectrum of fresh culture medium (Dulbecco's modified Eagle's medium containing 10% fetal bovine serum), which contains the essential nutrients including glucose, amino acids, vitamins, inorganic salts to provides a rich and balanced nutrient environment for the growth of irradiated MCF-7 cancer cells.

The Raman spectrum of fresh culture medium ranging from 300-1400 cm^{-1} (shown in **Figure 4.1**) revealed several significant peaks. Possible attributions for these peaks could be vibrations of the C-C bond in phenylalanine[36] at 530 cm^{-1}, acetoacetate[37] at 573 cm^{-1}, amino acid histidine[37] and phospholipids[37] at 654 cm^{-1}, C-H bending vibrations in the methyl and methylene groups of amino acids, lipids[36] at 718 cm^{-1}, C-C and C-N stretching vibrations in the amino acid phenylalanine[38] at 1009 cm^{-1}, symmetric stretching vibration of the phosphate group in nucleic acids[36] at 1094 cm^{-1}, and amide III band of proteins[39] at 1328 cm^{-1}.

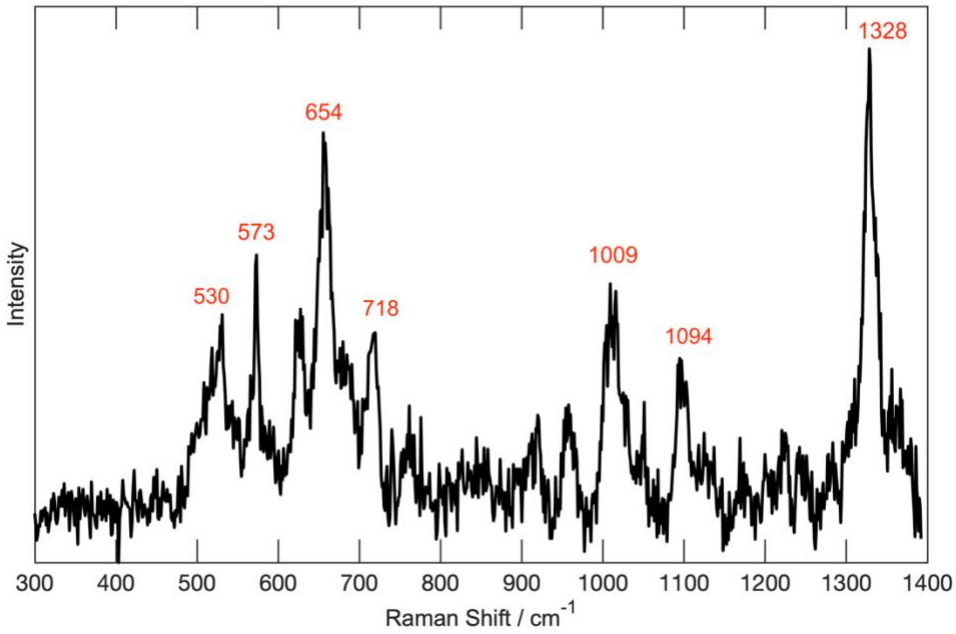

Figure 4.1. The Raman spectrum of fresh culture medium (Dulbecco's modified Eagle's medium containing 10% fetal bovine serum).

During the 24 hours post-irradiation, the irradiated cells absorbed a portion of the fresh culture medium and released their metabolisms into the extracellular environment. The SERS spectra of the supernatant samples from irradiated MCF-7 cells at different doses were collected one day after ionizing radiation and presented in **Figure 4.2**. Compared with the Raman spectrum of fresh culture medium, a strong broad band at 654 cm^{-1} was still present, while the bands at 573 cm^{-1}, 1009 cm^{-1}, and 1328 cm^{-1}were relatively weak in the SERS spectra of supernatant samples from irradiated and control cancer cells. This observation suggests that a certain percentage of irradiated cancer cells survived after ionizing radiation and maintained their interaction with the culture medium. Meanwhile, a new band at 725 cm^{-1} is observed, which can be assigned to the presence of hypoxanthine[40]

presenting in the extracellular environment of irradiated cells. This feature was observed among the one control group and two dose groups, and it will be further discussed.

The PCA analysis presented in **Figure 4.3** did not show the obvious separation of data points between the irradiated groups and control groups with 19.46% variance on PC1 and 11.02% variance on PC2. **Figure 4.4** shows the loading plot of PC1 and PC2, revealing that the band at 654 cm^{-1}, which corresponds to histidine and phospholipids from the culture medium, is the main contributor to the small variance observed. This suggests that there is little difference in the amount of these two nutrients in the spent medium among the three groups. In conclusion, there appears to be no significant difference in metabolism between the control cells and irradiated cells one day after ionizing radiation.

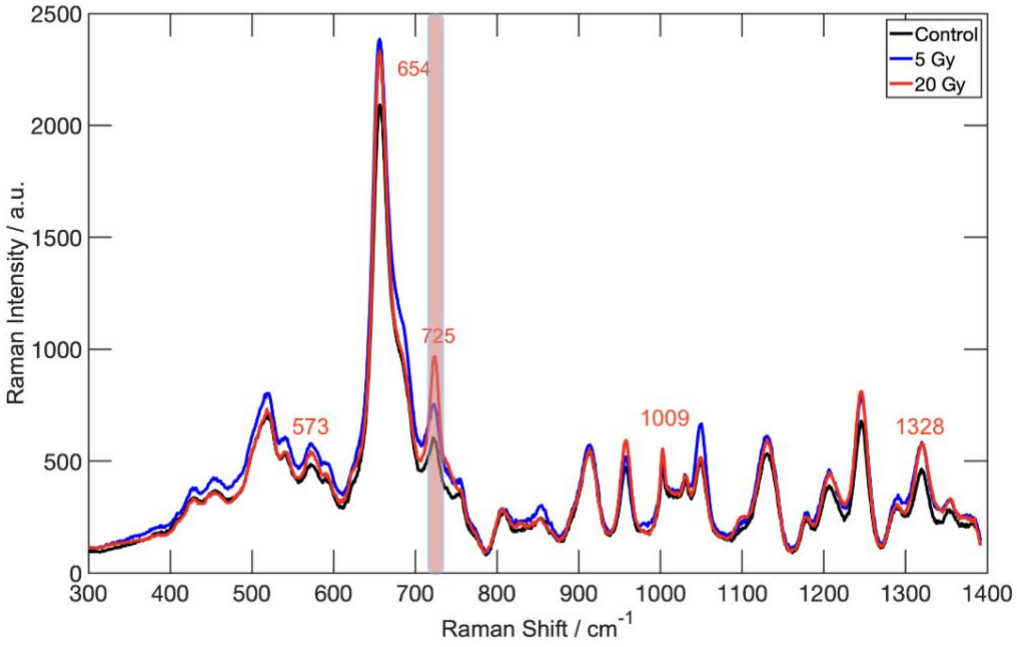

Figure 4.2. SERS spectra of irradiated MCF-7 cell supernatant samples 1 day after ionizing radiation at different intensity.

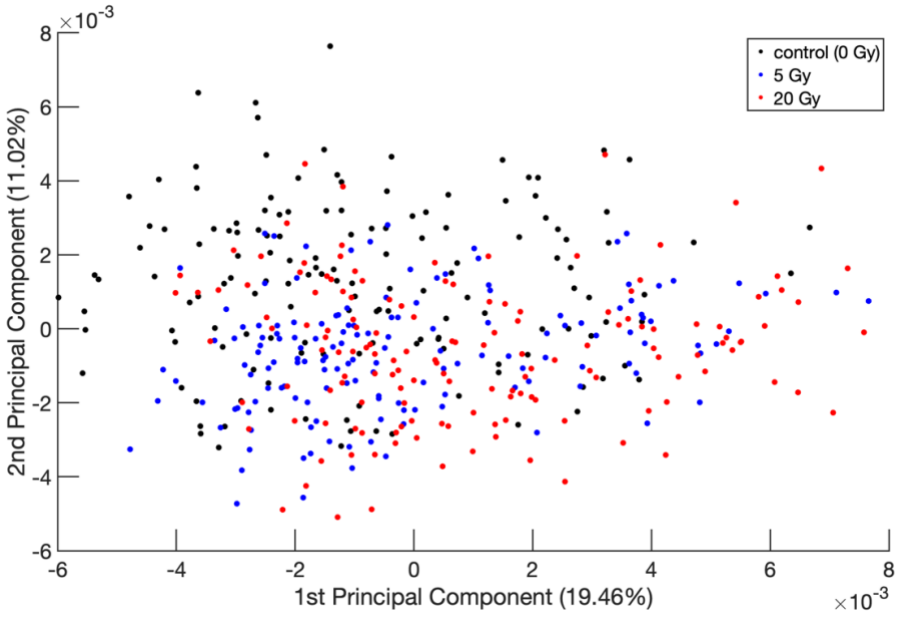

Figure 4.3. 2-D principal component analysis of supernatant samples 1 day after ionizing radiation at different dose intensity.

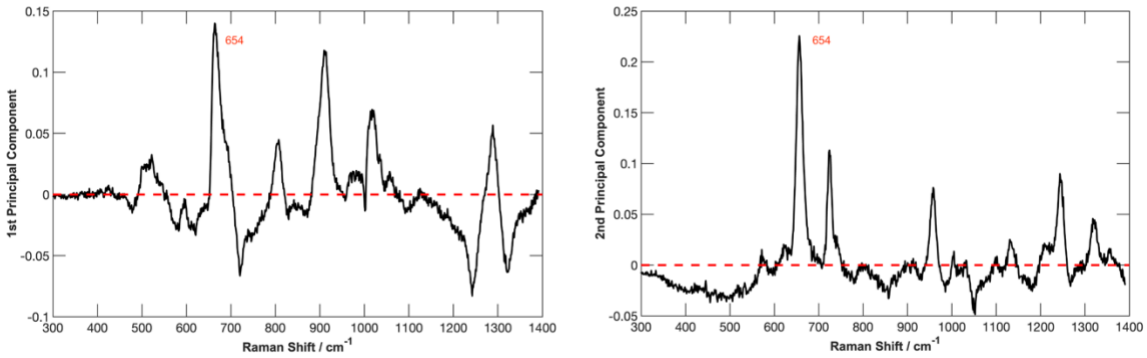

Figure 4.4. Loading plot on PC1 and PC2 in PCA of supernatant samples 1 day after ionizing radiation at different dose intensity.

4.1.2 SERS Results on Day 4

The SERS spectra of the supernatant samples from irradiated MCF-7 cells at different doses were collected 4 days after ionizing radiation and presented in **Figure 4.5**. It is evident that the intensity of the peak at 654 cm^{-1} varies across the three groups, with stronger doses exhibiting a correspondingly stronger peak intensity. However, the band at

725 cm^{-1} is not as pronounced as it was in the SERS spectra taken one day after ionizing radiation.

According to the PCA in **Figure 4.6**, a slight separation tendency between irradiated and control groups can be observed along the PC1 dimension, accounting for 22.95% of the variance. Most of the control data points appear on the positive side on the PC1 dimension, while a portion of the irradiated sample data points appears on the negative side. The peaks at 654 cm^{-1} and 1243 cm^{-1} are mainly responsible for this difference, as seen in the loading plot of the first and second components in **Figure 4.7**. As previously mentioned in the Raman spectrum analysis of the fresh culture medium, the presence of histidine and phospholipids account for the peak observed at 654 cm^{-1} and these molecules originated from the culture medium rather than from cell metabolisms. This suggests that cells exposed to different doses exhibited varying abilities to interact with the extracellular environment at the time of measurement. Specifically, cells exposed to low intensity doses were able to absorb more histidine and phospholipids from the medium, resulting in a lower intensity of the 654 cm^{-1} peak in the SERS spectra of supernatant samples. This observation is consistent with the expectation that cells exposed to lower doses, such as 5 Gy, would exhibit greater viability than those exposed to higher doses, such as 20 Gy. The peak at 1243 cm^{-1} is related to the presence of nucleic acids and nucleotides and will be discussed in the SERS spectra on day 12 following ionizing radiation.

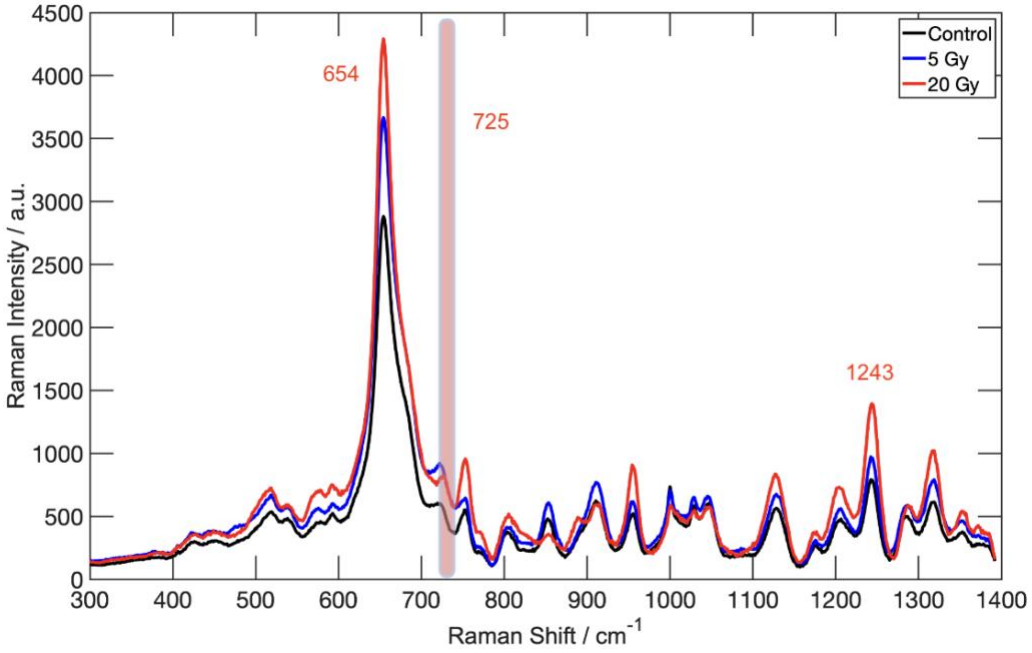

Figure 4.5. SERS spectra of irradiated MCF-7 cell supernatant samples 4 days after ionizing radiation at different intensity.

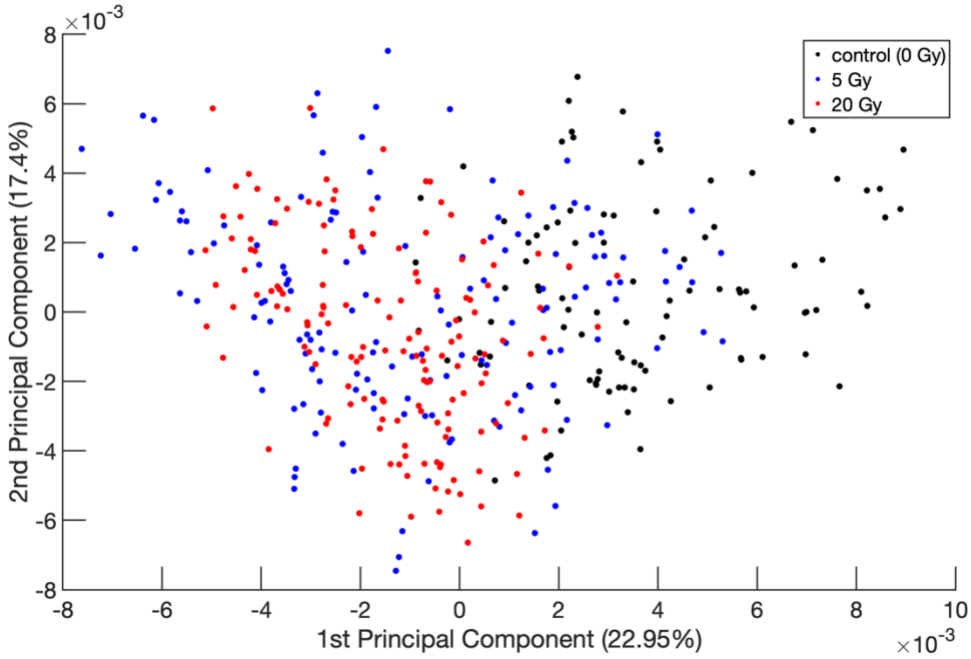

Figure 4.6. 2-D principal component analysis of supernatant samples 4 days after ionizing radiation at different dose intensity.

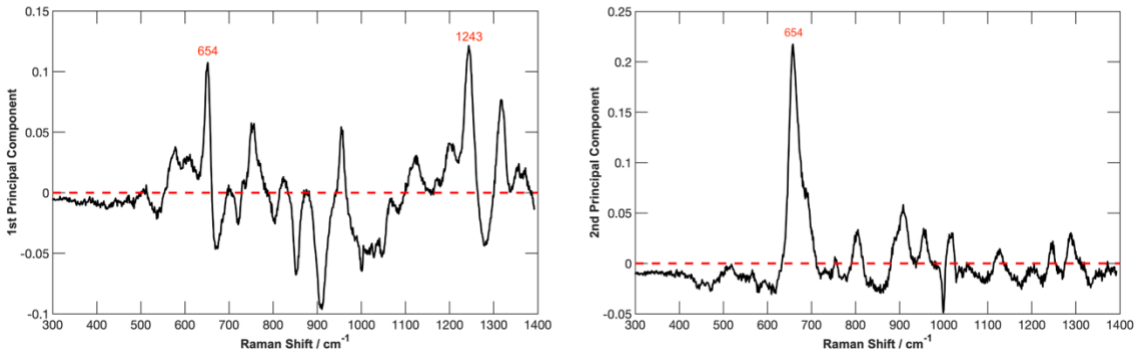

Figure 4.7. Loading plot on PC1 and PC2 in PCA of supernatant samples 4 days after ionizing radiation at different dose intensity.

4.1.3 SERS Results on Day 8

On the eighth day following ionizing radiation, the spectral feature emerged again in the irradiated groups with a clear band detected at 725 cm^{-1}, as shown in **Figure 4.8**. The PCA visualization results in **Figure 4.9** revealed a relatively obvious separation of data points between the control and irradiated groups. Specifically, the data points on the positive side of the PC1 dimension represented the irradiated samples while those on the negative side represented the control samples. Meanwhile, the PC1 loading plot in **Figure 4.10** showed that the peak at 725 cm^{-1} had a large positive loading value, suggesting that this peak was one of the main contributors to the difference between the control and irradiated groups.

The peak at 725 cm^{-1} was potentially responsible for the metabolism of hypoxanthine, which is a naturally occurring purine base; a building block of DNA and RNA.[41] It is a derivative of the purine base, adenine, with one of its nitrogen atoms replaced by a carbon atom. Hypoxanthine is also a breakdown product of purine nucleotides in the body, which are produced during the metabolism of certain foods and the turnover of

cellular nucleic acids.[42] Plou et al. discovered that the extracellular presence of hypoxanthine could be effectively identified in HeLa cells when exposed to a range of stress conditions, including high concentrations of hydrogen peroxide and staurosporine.[40] Therefore, the appearance of this peak at 725 cm^{-1} in the SERS spectra (**Figure 4.2**) of the control cells on the first day can be attributed to the transfer processes that control cells also underwent. These transfer processes involved the detachment of the cells, which could have caused a stress condition and the release of hypoxanthine from cells.

This discovery of a new peak at 725 cm^{-1} suggests that hypoxanthine may be a potential biomarker for cancer cellular stress response. The identification of hypoxanthine in extracellular fluids by SERS could be a useful tool for the potential clinical application in improving cancer diagnosis, monitoring, and treatment. Firstly, it could serve as a biomarker for the effectiveness of radiotherapy in cancer patients. By measuring the levels of hypoxanthine in the extracellular environment of cancer cells, clinicians could monitor the response of cancer cells to ionizing radiation and adjust treatment plans accordingly. For example, if hypoxanthine levels remain low despite several rounds of radiotherapy, it may be necessary to increase the intensity of radiation dose or switch to an alternative treatment strategy. On the other hand, based on our experimental results, it appears that radiotherapy may not produce immediate results. However, if a certain amount of hypoxanthine is detected 1-2 weeks after treatment, we can conclude that radiotherapy has had a certain level of effectiveness. Secondly, targeting hypoxanthine metabolism could be a potential therapeutic strategy for cancer treatment. By promoting the release of hypoxanthine or activating its downstream effects, it may be possible to reduce the risk of treatment resistance and improve the efficacy of radiotherapy.

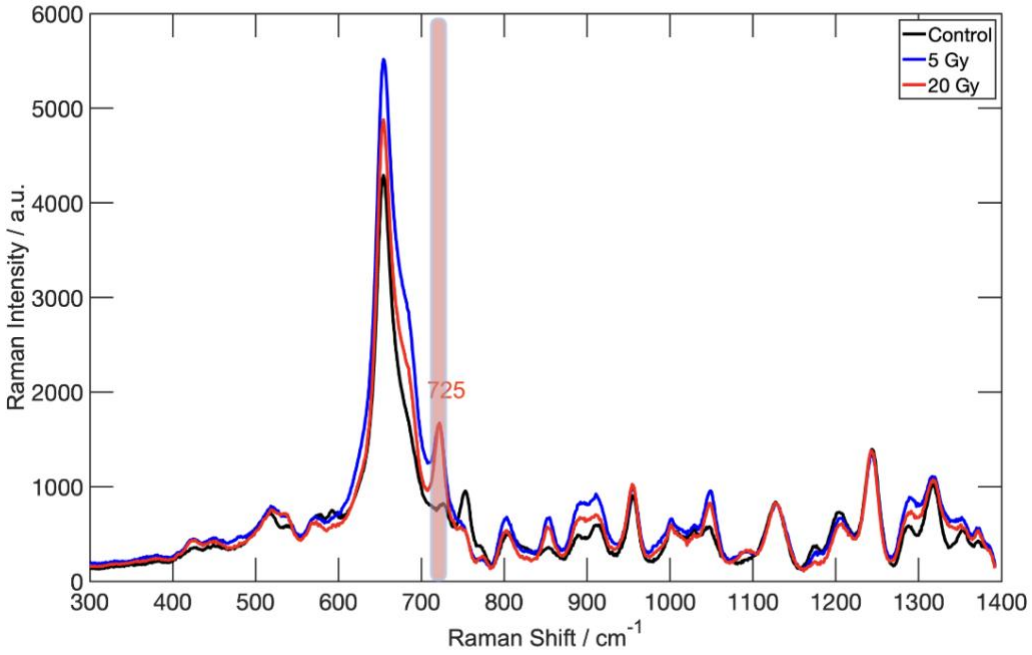

Figure 4.8. SERS spectra of irradiated MCF-7 cell supernatant samples 8 days after ionizing radiation at different intensities.

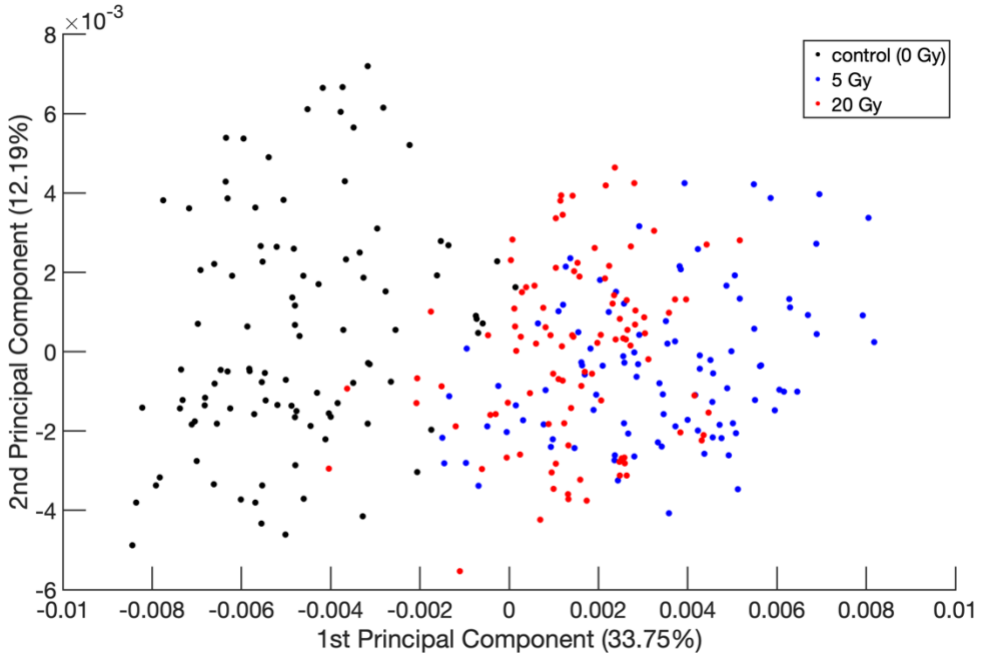

Figure 4.9. 2-D principal component analysis of supernatant samples 8 days after ionizing radiation at different dose intensity.

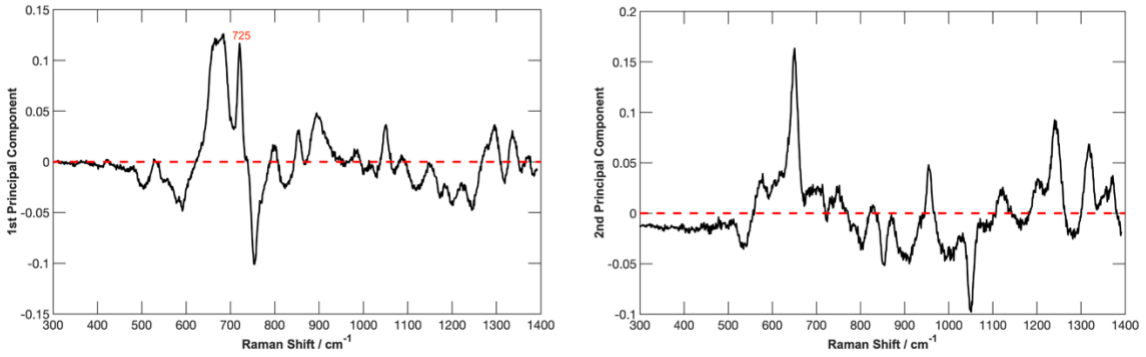

Figure 4.10. Loading plot on PC1 and PC2 in PCA of supernatant samples 8 days after ionizing radiation at different dose intensity.

4.1.4 SERS Results on Day 12

Significant differences were observed in the SERS spectra among the three dose intensity groups on day 12 after the ionizing radiation. The SERS data (shown in **Figure 4.11**) present a prominent peak at 725 cm^{-1} in the 20 Gy irradiated sample. The PCA (presented in **Figure 4.12**) shows the complete separation of data points of three groups with 54.52% of the variance for the first principal component. The loading plot of the first component (shown in **Figure 4.13**) revealed that the peak at 725 cm^{-1} with a large positive loading value was the main contributor to the variance.

The SERS spectra (**Figure 4.11**) suggest that the strong ionizing radiation dose has a huge impact on the metabolism of MCF-7 cells (beyond just the increase in the feature at 725 cm^{-1}). The behaviour of other SERS peaks in different spectral regions also suggest significant changes in the extracellular milieu when cells get irradiated. In particular, the intensity of Raman peaks at 801, 954, 1093, 1128, 1207, 1243, 1319, and 1370 cm^{-1} increased with the irradiation dose on day 12 following ionizing radiation. These Raman peaks have been associated with various biomolecules and metabolic processes that are

involved in the radiation response of cancer cells. One potential interpretation of these peaks is that they are related to the presence of nucleic acids and nucleotides, which are the building blocks of DNA and RNA.[43,44] The peak at 801 cm^{-1} is often attributed to the guanine ring breathing mode of nucleic acids,[45] while the peaks at 1093 cm^{-1} and 1319 cm^{-1} have been linked to the C-C stretching vibrations of nucleic acids.[46] The peaks at 1207 cm^{-1} and 1243 cm^{-1} are also associated with nucleic acids, specifically with the symmetric phosphate stretching mode of DNA and RNA. [47] Other potential interpretations of these peaks include their association with lipid metabolism, protein conformational changes, and various other metabolic processes that are altered in irradiated cells and lead to changes in the extracellular milieu.

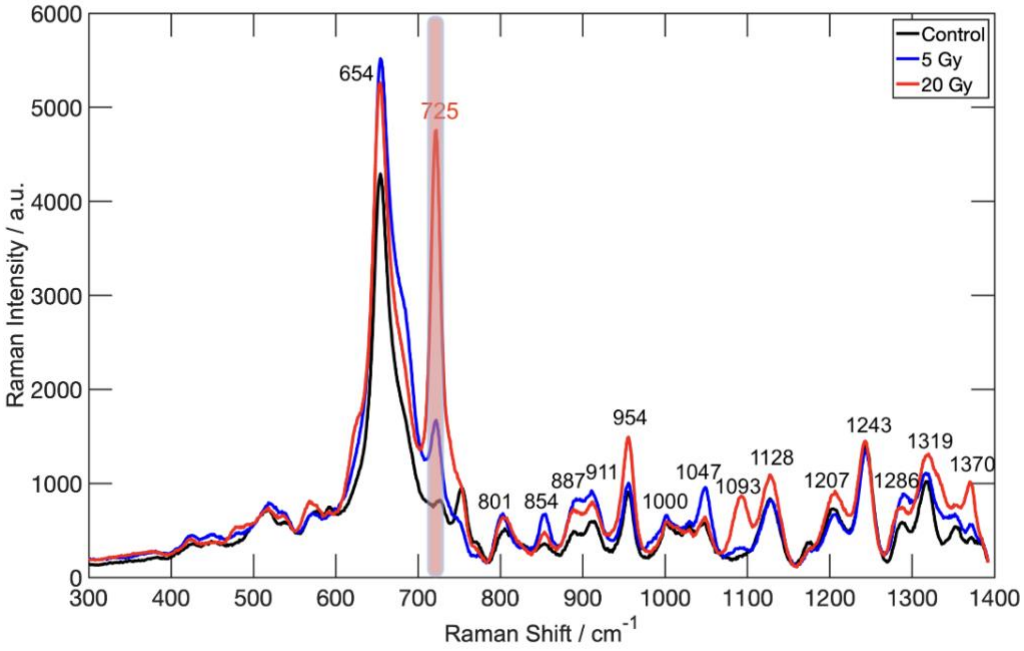

Figure 4.11. SERS spectra of irradiated MCF-7 cell supernatant samples 12 days after ionizing radiation at different intensity.

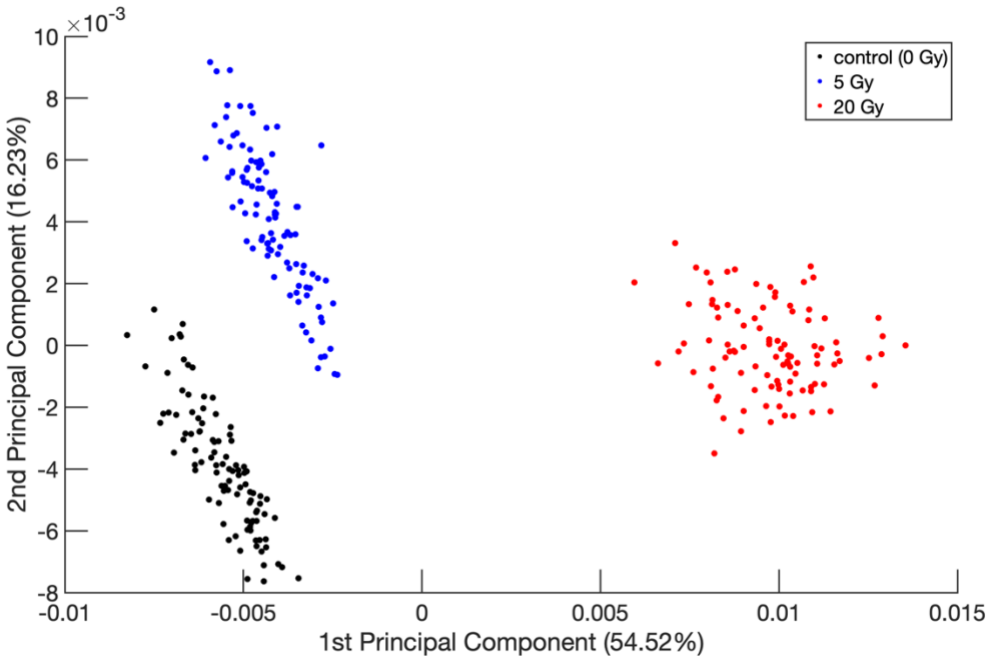

Figure 4.12. 2-D principal component analysis of supernatant samples 12 days after ionizing radiation at different dose intensity.

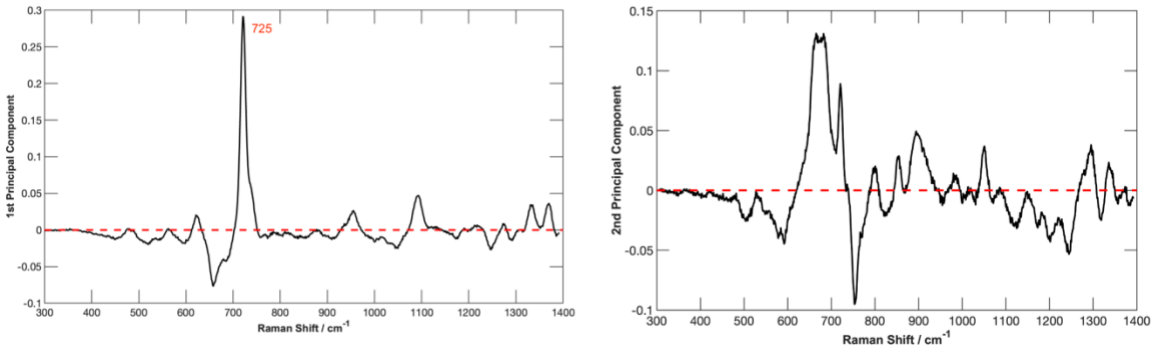

Figure 4.13. Loading plot on PC1 and PC2 in PCA of supernatant samples 12 days after ionizing radiation at different dose intensity.

4.2 Identification of the Origin of the Peak at 725 cm^{-1}

In the previous section, it was demonstrated that the irradiated samples displayed a prominent peak at 725 cm^{-1} on day 12 following ionizing radiation. That peak may potentially be attributed to hypoxanthine, as per the research conducted by Plou et al.[40] on

cancer cells under stressful conditions. Another potential candidate for this peak is inosine, a metabolite that shares structural similarities with hypoxanthine. The structure of hypoxanthine and inosine is shown in **Figure 4.14**. Hypoxanthine and inosine both contain a six-membered pyrimidine ring fused to a five-membered imidazole ring, forming the purine base. The difference is that hypoxanthine contains only the purine base, while inosine contains the purine base plus a ribose sugar. Furthermore, it is noted in the literature[48] that the Raman spectrum of hypoxanthine typically displays a peak at approximately 725 cm^{-1}, which corresponds to the stretching of the bond between the carbon atom located at position 8 and the nitrogen atom located at position 9 in the purine ring. SERS spectra of both hypoxanthine and inosine solutions were obtained using our coffee ring-based substrate. The goal was to determine which of these metabolites would be the dominant species in the extracellular medium of the irradiated cells.

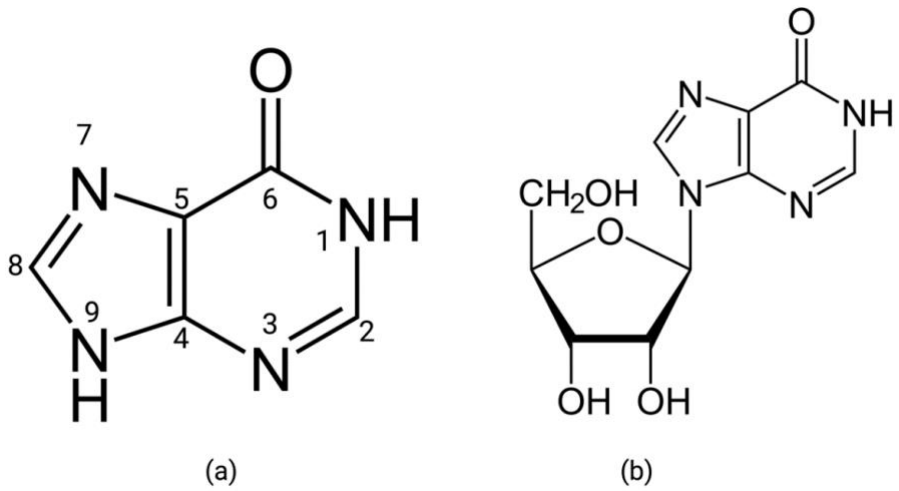

Figure 4.14. Chemical structures of hypoxanthine (a) and inosine (b).

10 μM of hypoxanthine and inosine aqueous solution were spiked on our coffee ring-based substrate and then the SERS spectrum was collected. **Figure 4.15** shows the

spectra after baseline removal and normalization within the range from 600 cm^{-1} to 1400 cm^{-1}.

In addition to the peak at 725 cm^{-1}, assigned to the stretching of the C-N stretching of the ring, the Raman spectrum of hypoxanthine (**Figure 4.15** (a)) shows several other features. Specifically, the peak at 1096 cm^{-1} corresponds to the C-N stretching mode in the pyrimidine ring of hypoxanthine, while the peak at 1280 cm^{-1} corresponds to the C-H bending mode in the pyrimidine ring. The peak at 1306 cm^{-1} corresponds to the C-N stretching mode in the imidazole ring of hypoxanthine, and the peak at 1332 cm^{-1} corresponds to the C-H bending mode in the pyrimidine ring.[36]

In the SERS spectrum of inosine solution, shown in **Figure 4.15** (b), the peak at 738 cm^{-1} corresponds to the C4N7H deformation mode in the pyrimidine ring, while the peak at 1052 cm^{-1} corresponds to the C-C stretching mode in the ribose sugar unit of the molecule. Additionally, a wide peak at 1318 cm^{-1} is observed in the inosine Raman spectrum, which is a combination band resulting from several different modes, including the C2N3H bending mode in the pyrimidine ring and the C-O stretching mode in the ribose sugar.[36]

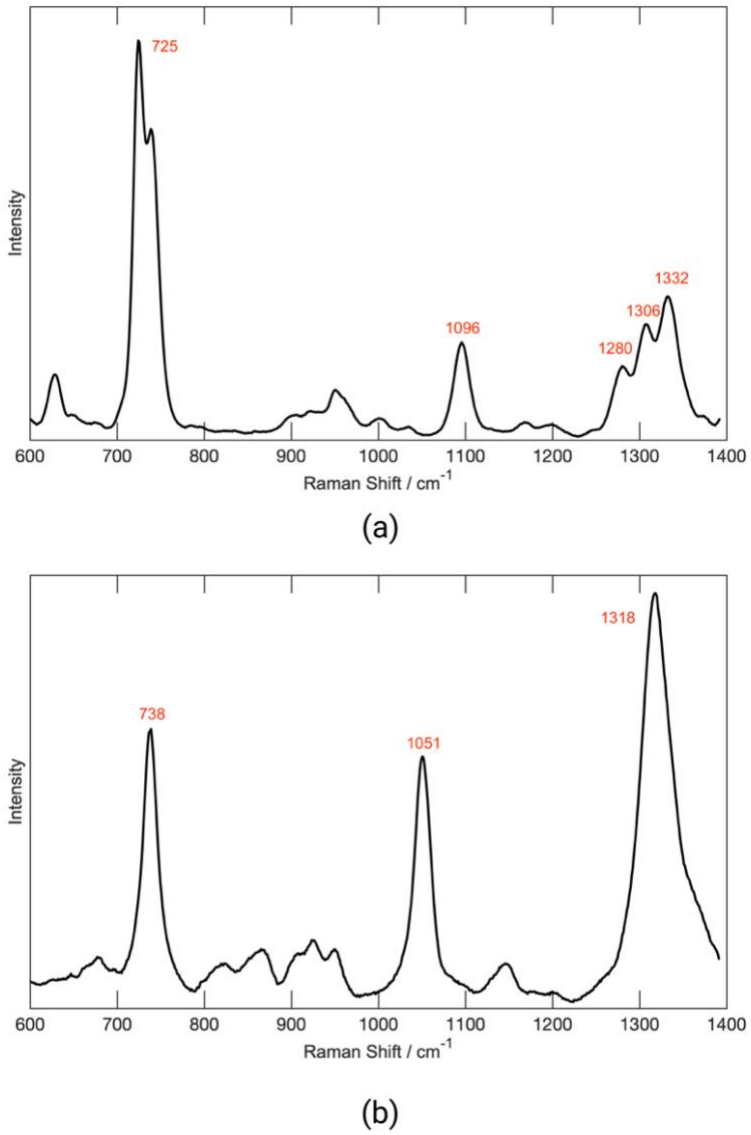

Figure 4.15. SERS spectra of 10 μM hypoxanthine (a) and inosine solutions (b).

Although the peak at 725 cm^{-1} in the hypoxanthine solution corresponds to the same peak in the irradiated cell supernatant samples, it is worth performing PCA between the hypoxanthine solution spectrum and 20 Gy irradiated sample spectrum on day 12 to consider other peaks, such as 1096, 1280, 1306, and 1332 cm^{-1} in the hypoxanthine spectrum. The loading plot of the second principal component (only 0.63% variance),

presented in **Figure 4.16** reveals that the loading values of the peak areas at 1096, 1280, 1306, and 1332 cm^{-1} are almost zero, indicating their weak influence on the component. Therefore, it can be concluded that hypoxanthine is the primary metabolite responsible for the peak at 725 cm^{-1}.

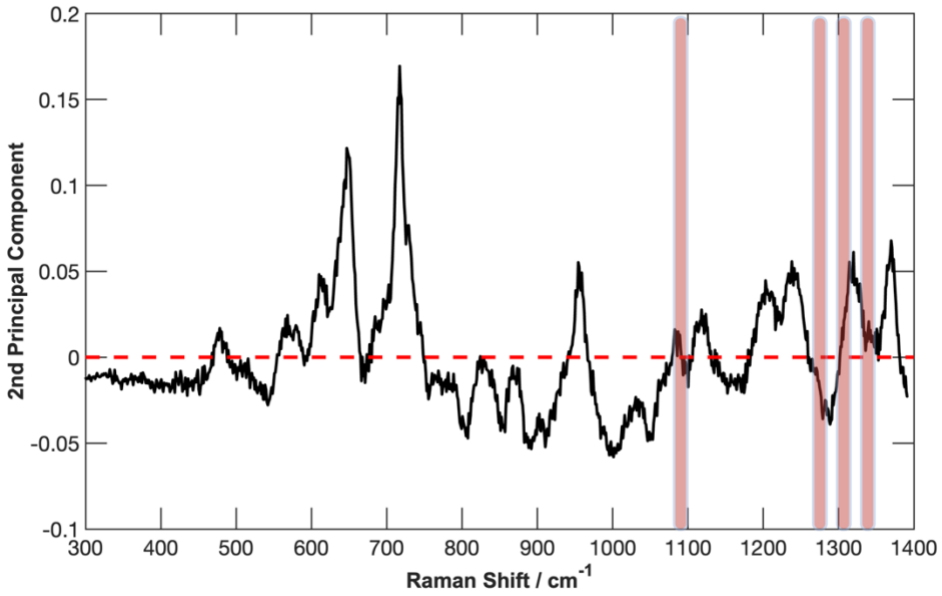

Figure 4.16. Loading plot on PC2 in PCA of hypoxanthine solution spectrum and 20 Gy (day 12) irradiated sample spectrum. The loading value of the four selected peak areas is close to 0.

In Chapter 2.2, the fundamental mechanism of how radiation therapy works on cancer cells was explained. Essentially, ionizing radiation damages the DNA structure in cancer cells. Connecting this mechanism with the discovery that the cells release hypoxanthine into their extracellular milieu after ionizing radiation can be done by considering that cancer cells exposure to ionizing radiation cause DNA damage at various time points, triggering the activation of various signalling pathways that lead to cellular stress and injury. In response to this stress or injury, the cancer cells release ATP into the

extracellular space.[49,50] ATP is primarily present at high concentrations intracellularly, and in very low concentrations in the extracellular compartment of tissues. It serves as the key energy currency within cells, as well as a ubiquitous extracellular messenger and a prototypical DAMP (damage-associated molecular pattern).[49,51] The multi-step enzymatic process of ATP conversion to hypoxanthine involves several extracellular enzymes on the cell surface.[50] Both conversions from ATP to ADP and ADP to AMP involve the enzyme ecto-nucleoside triphosphate diphosphohydrolase (ENTPDase).[50] The produced AMP then can be deaminated by the enzyme adenosine deaminase (ADA) to form inosine.[50] Inosine is then further metabolized to hypoxanthine by the enzyme purine nucleoside phosphorylase (PNP).[50] These enzymes play important roles in regulating the levels of extracellular purine nucleotides and metabolites, which can have important physiological and pathophysiological effects.

4.3 Investigation of the Cell Apoptosis

Upon identifying hypoxanthine as the primary contributor to the 725 cm^{-1} peak and understanding the potential mechanism for its release into the extracellular milieu, the next step is to investigate whether cells remained viable or underwent apoptosis during the production of hypoxanthine. Chapter 3.5 demonstrated the steps for using the caspase-3 Z-DEVD-FMK inhibitor to enhance cell viability, and showcased how cell viability was assessed using the Trypan Blue Exclusion Assay. **Error! Reference source not found.** and **Error! Reference source not found.** show the living cell ratio of irradiated cells that received caspase-3 inhibitor treatment and control (non-treatment) following 5 and 20 Gy ionizing radiation, respectively.

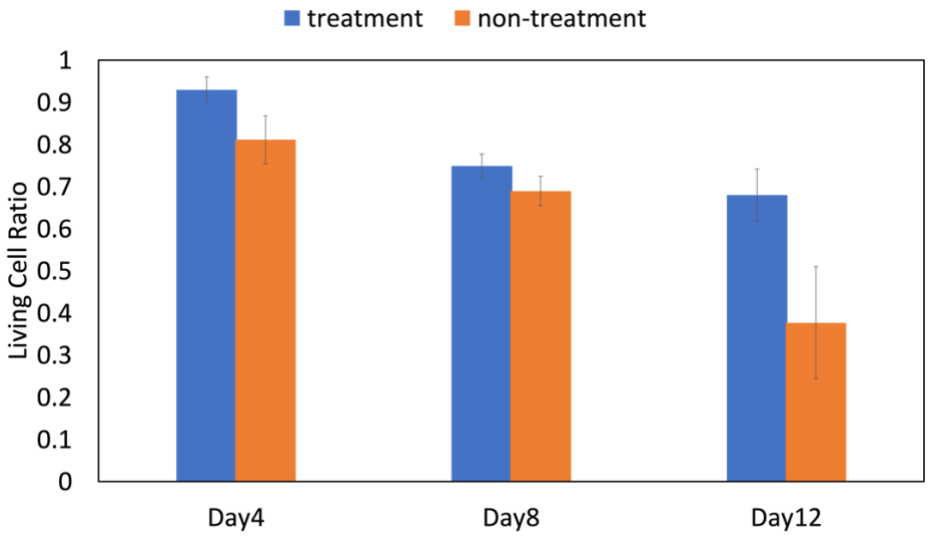

Figure 4.17. Living cell ratio of 5 Gy irradiated cells with treatment and control on 4, 8, and 12 days after ionizing radiation. The error bar is represented by the standard deviation. the t-test yielded p-values of 0.018, 0.037, and 0.001 for the treatment group compared to the non-treatment group.

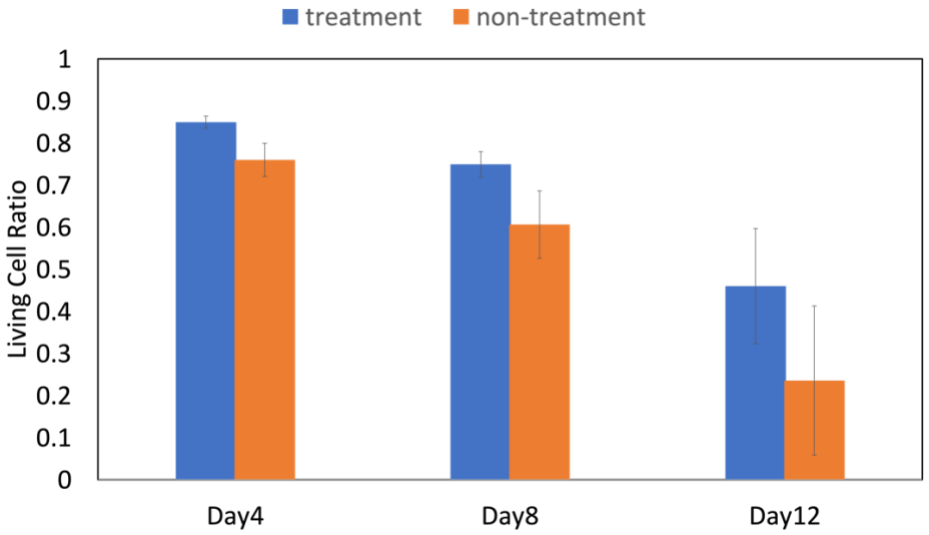

Figure 4.18. Living cell ratio of 20 Gy irradiated cells with treatment and control on 4, 8, and 12 days after ionizing radiation. The error bar is represented by the standard deviation. The t-test yielded p-values of 0.046, 0.013, and 0.009 for the treatment group compared to the control group.

As expected, the number of living cells decreased over time in both the 5 Gy and 20 Gy irradiated cell groups. Meanwhile, when treated with caspase-3 inhibitor, the number of living cells was higher compared to those without treatment. This is evidence that the caspase inhibitor blocked cell death to a certain degree. Furthermore, the t-test was used to determine whether there is a significant difference between the means of treatment and non-treatment groups. The t-test is applicable when comparing two independent groups or when comparing the same group under two different conditions. The results of the t-test provide additional support for the conclusion that the caspase inhibitor improves cell viability. In the case of the 5 Gy irradiated cells, the t-test yielded p-values of 0.018, 0.037, and 0.001 for the treatment group compared to the control group. Similarly, for the 20 Gy irradiated cells, the p-values were 0.046, 0.013, and 0.009 for the treatment group compared to the control group. Since all of these p-values are smaller than the significance level of 0.05, it can be concluded that there is a significant difference in cell viability between the treatment and control groups.

SERS spectra were obtained from the supernatant of both treatment and control groups to determine the presence of the hypoxanthine peak in their respective spectrum. The peak observed at 674 cm^{-1} was confirmed to be from the DMSO (DMSO SERS spectrum was shown in **Figure 4.19**), which is associated with the C–S–C symmetric stretching vibration.[52]

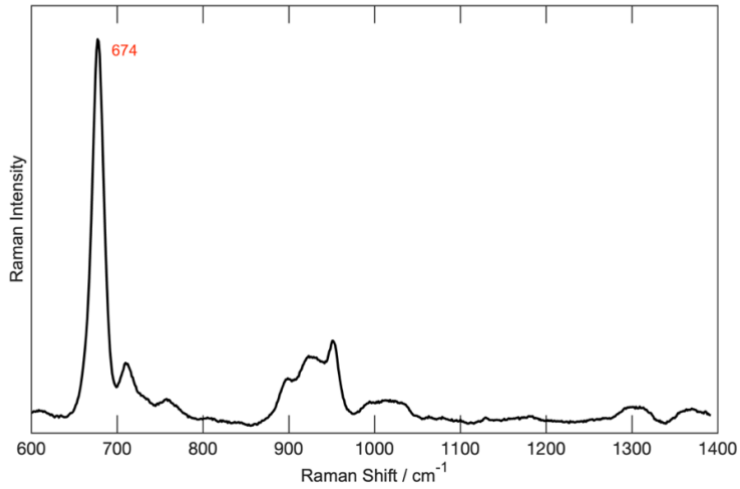

Figure 4.19. SERS spectrum of DMSO.

For 5 Gy irradiated cell supernatant samples, the treatment group shows a weak peak at 725 cm^{-1} on day 4, 8, and 12 post-ionizing radiations. Additionally, it was noted that the peak on day 12 was even weaker than those on day 4 and day 8, which suggests a reduction in the release of hypoxanthine on day 12. In contrast, the control group shows a gradually increasing peak at 725 cm^{-1} over time, with a relatively strong signal on day 12 (shown in **Figure 4.20** and **Figure 4.21**). It can be observed that the control group produced a greater amount of hypoxanthine than the treatment group on day 12.

By performing the PCA on the SERS spectra of both treatment and control groups on day 12, it was observed that PC1 and PC2 accounted for 29.76% and 17.36% of the variance, respectively. The loading plot on PC1 identified a peak at 725 cm^{-1} with a negative loading value close to -0.1 (as shown in **Figure 4.22**), indicating that this peak was one of the primary contributors that influenced the component. In conclusion, it can be inferred that the release of hypoxanthine in the treatment group was lower than that in the control group for the 5 Gy irradiated cell supernatant sample.

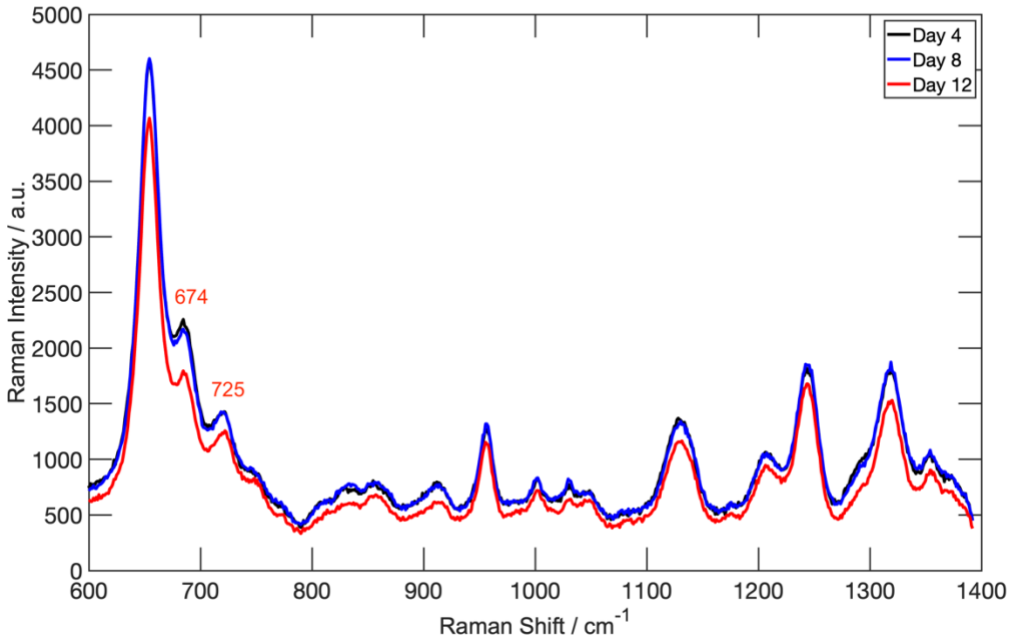

Figure 4.20. SERS spectra of 5 Gy irradiated MCF-7 cell supernatant samples with caspase inhibitor treatment 4, 8, 12 days after ionizing radiation.

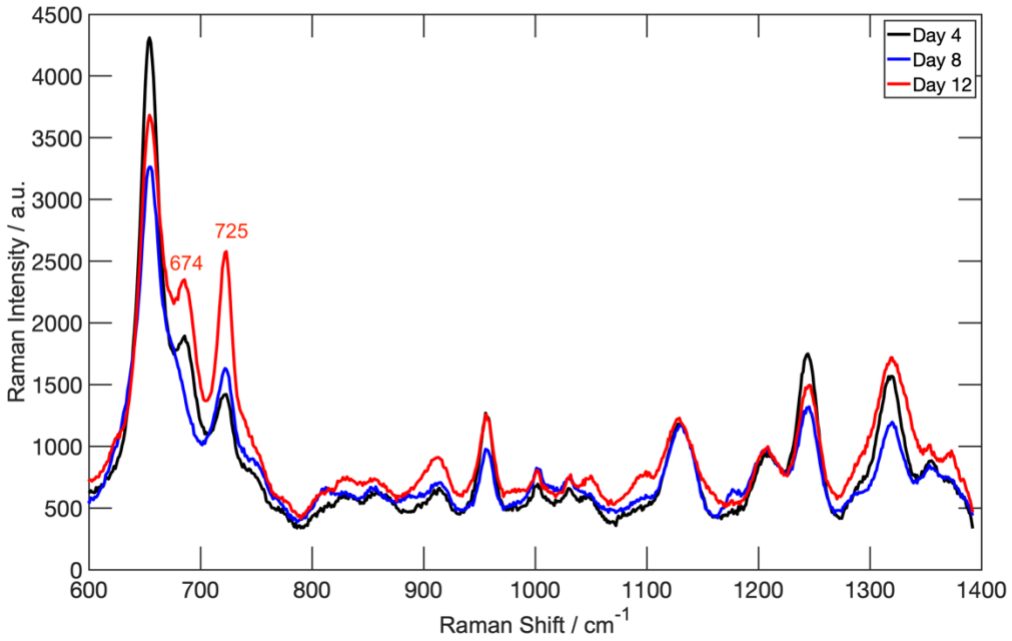

Figure 4.21. SERS spectra of 5 Gy irradiated MCF-7 cell supernatant samples without caspase inhibitor treatment 4, 8, 12 days after ionizing radiation.

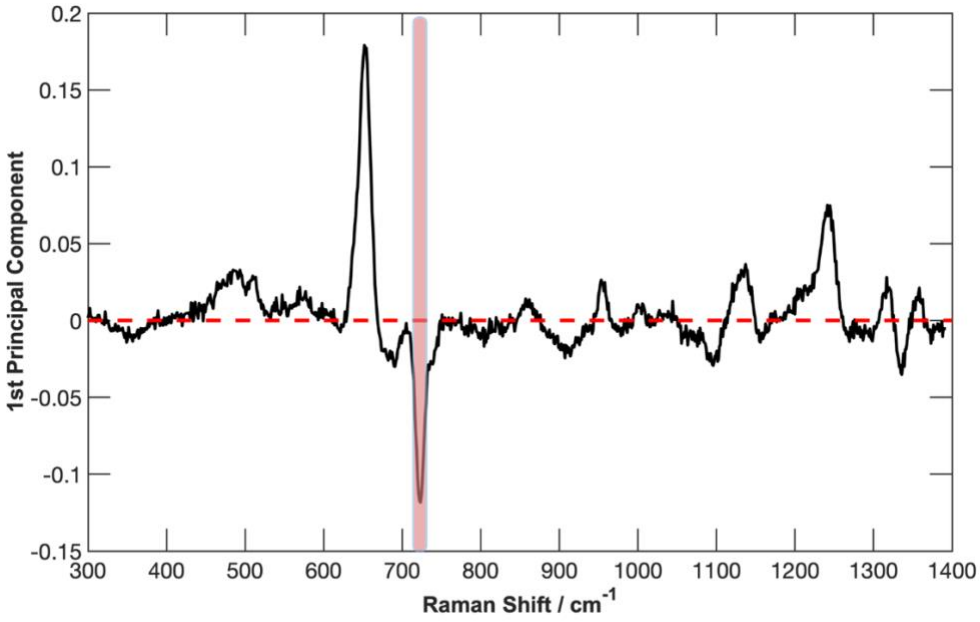

Figure 4.22. The loading plot on PC1 revealed the peak at 725 cm^{-1} with a loading value of -0.12 in the PCA of SERS spectra obtained from 5 Gy irradiated MCF-7 cell supernatant samples with and without treatment on day 12 post-ionizing radiation.

We have a similar conclusion for the 20 Gy irradiated cell supernatant samples. For both treatment and control groups, the peak intensity at 725 cm^{-1} increased over time (**Figure 4.23** and **Figure 4.24**). The treatment group shows relatively lower intensity at the same time points, especially on day 12, suggesting that the release of hypoxanthine in the treatment group is also less than in the control group. The findings obtained from the cell viability test and SERS analysis of both treatment and control groups suggest that there is an association between reduced cell viability and increased hypoxanthine release in the two weeks following ionizing radiation, regardless of the dose intensity (5 Gy or 20 Gy). Therefore, it can be concluded that the production of hypoxanthine in the extracellular environment is a marker for cell apoptosis.

While there has been extensive research on hypoxanthine as a radiation biomarker in recent years, alternative analytical techniques have been employed. Chen et al. showed the detection of two radiation biomarkers, trimethyl-L-lysine and hypoxanthine in the nonhuman primate urine samples which were exposed to a 10 Gy dose through Differential mobility spectrometry-mass spectrometry (DMS-MS) and liquid chromatography-mass spectrometry (LC-MS).[53] Johnson et al. also discovered 13 biomarkers of radiation including hypoxanthine in the nonhuman primate urine sample which was exposed to different doses of ionizing radiation through MS.[54] In conclusion, this study suggests that the hypoxanthine can be used as a potential radiation biomarker detected by SERS for the MCF-7 cancer cell line exposed to ionizing radiation. Therefore, the future application of SERS as an analytical technique to identify hypoxanthine as a radiation biomarker in human-derived samples appears to hold great potential.

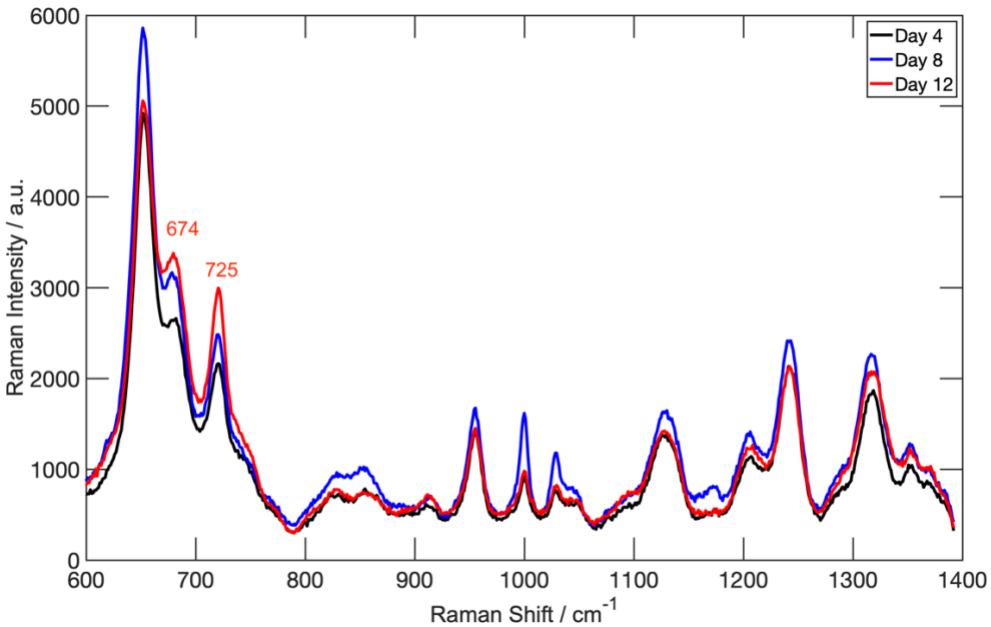

Figure 4.23. SERS spectra of 20 Gy irradiated MCF-7 cell supernatant samples with caspase inhibitor treatment 4, 8, 12 days after ionizing radiation.

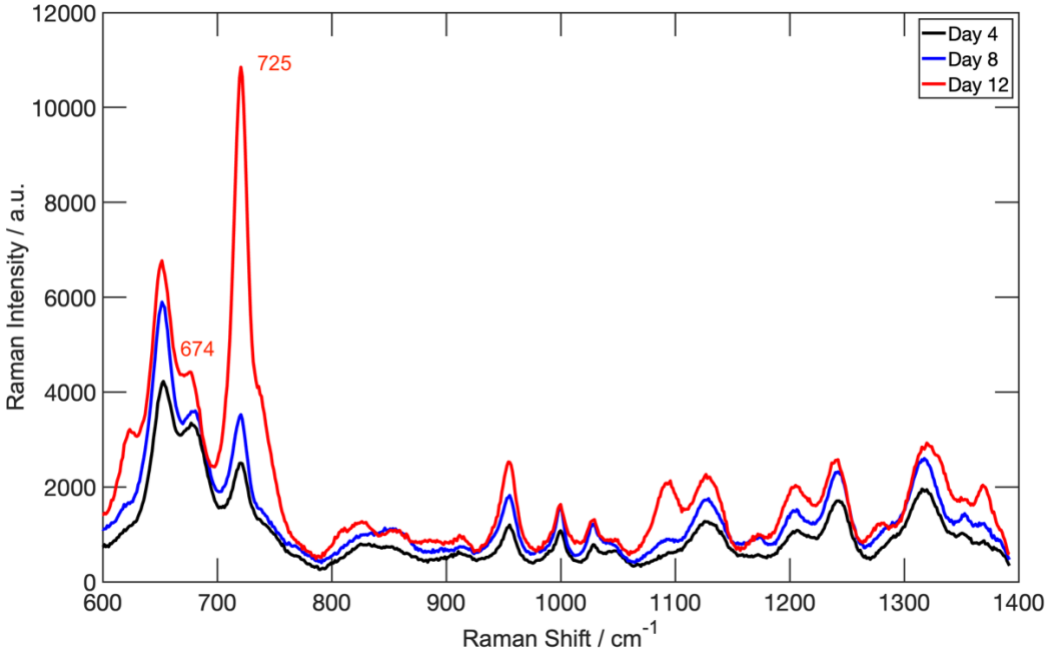

Figure 4.24. SERS spectra of 20 Gy irradiated MCF-7 cell supernatant samples without caspase inhibitor treatment 4, 8, 12 days after ionizing radiation.

Chapter 5. Conclusion and Future Work

This present thesis reveals significant metabolic alterations in the extracellular environment of the MCF-7 breast cancer cell line following radiation therapy, as determined by SERS. Notably, a new peak was detected at 725 cm^{-1} in the supernatant metabolism samples from the MCF-7 cells exposed to 5 and 20 Gy doses. Notably, in the case of the MCF-7 cells exposed to the 20 Gy dose, its intensity experienced a significant increase two weeks after irradiation, indicating a substantial change in metabolic activity at this time point. Further analysis identified hypoxanthine as the primary compound contributing to this peak at 725 cm^{-1}, with its presence linked to cellular apoptosis during the post-radiation stage. The identification of hypoxanthine in extracellular fluids could be a useful tool for the potential clinical application in improving cancer diagnosis, monitoring, and treatment. Meanwhile, these findings provide valuable insight into the metabolic changes induced by radiation therapy and highlight the potential of SERS as a tool for studying extracellular metabolic alterations in cancer cells.

Other techniques such as HPLC and GC-MS are used for the metabolites detection. They also offer excellent sensitivity, allowing for the detection of metabolites in complex samples. However, SERS has the advantage of high sensitivity in some cases. In general, SERS has demonstrated the capability to detect molecules at concentrations ranging from micromolar down to picomolar and even femtomolar levels. Sample preparation requirements can also differ among the SERS and other techniques. SERS typically requires a simpler sample preparation process compared to HPLC and GC-MS. For SERS, the analytes can be directly measured in complex biological samples, reducing the need for extensive extraction or derivatization steps. In contrast, HPLC and GC-MS often involve

laborious sample preparation procedures, including extraction, purification, and derivatization, to ensure analyte compatibility and separation.

In our forthcoming research, additional cancer cell lines may also be employed to understand their response to radiation therapy and compare the metabolites determined by SERS with the MCF-7 case studied in this thesis. We also plan to obtain serum samples from patients who have undergone radiation therapy at the BC Cancer Agency. These samples will be subjected to SERS measurements to investigate the potential use of hypoxanthine as a radiation biomarker in clinical settings. It is worth mentioning that working with clinical samples shows several challenges. Clinical samples often consist of not only cancer cells but also various types of normal cells, leading to increased complexity and heterogeneity in the analysis.

Bibliography

(1) *American Cancer Society. (2021). Breast Cancer*. https://www.cancer.org/cancer/breast-cancer.html.

(2) *World Health Organization. (2022, March 26). "Breast Cancer."* https://www.who.int/news-room/fact-sheets/detail/breast-cancer.

(3) Comșa, Ș.; Cîmpean, A. M.; Raica, M. The Story of MCF-7 Breast Cancer Cell Line: 40 Years of Experience in Research. *ANTICANCER Res.* **2015**.

(4) *MCF-7 Cell Line - an overview | ScienceDirect Topics*. https://www.sciencedirect.com/topics/medicine-and-dentistry/mcf-7-cell-line (accessed 2022-10-03).

(5) Tengku Din, T. A. D. A.-A.; Seeni, A.; Khairi, W.-N. M.; Shamsuddin, S.; Jaafar, H. Effects of Rapamycin on Cell Apoptosis in MCF-7 Human Breast Cancer Cells. *Asian Pac. J. Cancer Prev.* **2015**, *15* (24), 10659–10663. https://doi.org/10.7314/APJCP.2014.15.24.10659.

(6) Jamalzadeh, L.; Ghafoori, H.; Aghamaali, M.; Sariri, R. Induction of Apoptosis in Human Breast Cancer MCF-7 Cells by a SemiSynthetic Derivative of Artemisinin: A Caspase-Related Mechanism. *Iran. J. Biotechnol.* **2017**, *15* (3), 157–165. https://doi.org/10.15171/ijb.1567.

(7) *Progesterone receptor action: defining a role in breast cancer - PMC*. https://www.ncbi.nlm.nih.gov/pmc/articles/PMC3156468/ (accessed 2023-05-21).

(8) Zhang, X. H.-F.; Giuliano, M.; Trivedi, M. V.; Schiff, R.; Osborne, C. K. Metastasis Dormancy in Estrogen Receptor–Positive Breast Cancer. *Clin. Cancer Res.* **2013**, *19* (23), 6389–6397. https://doi.org/10.1158/1078-0432.CCR-13-0838.

(9) Gianfaldoni, S.; Gianfaldoni, R.; Wollina, U.; Lotti, J.; Tchernev, G.; Lotti, T. An Overview on Radiotherapy: From Its History to Its Current Applications in Dermatology. *Open Access Maced. J. Med. Sci.* **2017**, *5* (4), 521–525. https://doi.org/10.3889/oamjms.2017.122.

(10) Gasinska, A. The Contribution of Women to Radiobiology: Marie Curie and Beyond. *Rep. Pract. Oncol. Radiother.* **2016**, *21* (3), 250–258.

(11) Holsti, L. R. Development of Clinical Radiotherapy since 1896. *Acta Oncol.* **1995**, *34* (8), 995–1003.

(12) Baskar, R.; Dai, J.; Wenlong, N.; Yeo, R.; Yeoh, K.-W. Biological Response of Cancer Cells to Radiation Treatment. *Front. Mol. Biosci.* **2014**, *1*. https://doi.org/10.3389/fmolb.2014.00024.

(13) Borges, H. L.; Linden, R.; Wang, J. Y. DNA Damage-Induced Cell Death: Lessons from the Central Nervous System. *Cell Res.* **2008**, *18* (1), 17–26. https://doi.org/10.1038/cr.2007.110.

(14) Norbury, C. J.; Zhivotovsky, B. DNA Damage-Induced Apoptosis. *Oncogene* **2004**, *23* (16), 2797–2808.

(15) Roos, W. P.; Kaina, B. DNA Damage-Induced Cell Death by Apoptosis. *Trends Mol. Med.* **2006**, *12* (9), 440–450. https://doi.org/10.1016/j.molmed.2006.07.007.

(16) Wang, J. Y. Focus: Death: Cell Death Response to DNA Damage. *Yale J. Biol. Med.* **2019**, *92* (4), 771.

(17) Salinas, L.; Maldonado, E.; Navarro, R. Stress-Induced Germ Cell Apoptosis by a P53 Independent Pathway in Caenorhabditis Elegans. *Cell Death Differ.* **2006**, *13* (12), 2129–2139.

(18) Yu, J.; Zhang, L. No PUMA, No Death: Implications for P53-Dependent Apoptosis. *Cancer Cell* **2003**, *4* (4), 248–249.
(19) Abu-Qare, A. W.; Abou-Donia, M. B. Biomarkers of Apoptosis: Release of Cytochrome c, Activation of Caspase-3, Induction of 8-Hydroxy-2'-Deoxyguanosine, Increased 3-Nitrotyrosine, and Alteration of P53 Gene. *J. Toxicol. Environ. Health B Crit. Rev.* **2001**, *4* (3), 313–332.
(20) Hajra, K. M.; Liu, J. R. Apoptosome Dysfunction in Human Cancer. *Apoptosis* **2004**, *9*, 691–704.
(21) Shiri, R.; Yari, F.; Ahmadinejad, M.; Vaeli, S.; Tabatabaei, M. R. The Caspase-3 Inhibitor (Peptide Z-DEVD-FMK) Affects the Survival and Function of Platelets in Platelet Concentrate during Storage. *Blood Res.* **2014**, *49* (1), 49–53.
(22) Shi, Y. Caspase Activation, Inhibition, and Reactivation: A Mechanistic View. *Protein Sci. Publ. Protein Soc.* **2004**, *13* (8), 1979–1987. https://doi.org/10.1110/ps.04789804.
(23) Ghaderi, N.; Jung, J.; Brüningk, S. C.; Subramanian, A.; Nassour, L.; Peacock, J. A Century of Fractionated Radiotherapy: How Mathematical Oncology Can Break the Rules. *Int. J. Mol. Sci.* **2022**, *23* (3), 1316.
(24) Calvo, F. A.; Chera, B. S.; Zubizarreta, E.; Scalliet, P.; Prasad, R. R.; Quarneti, A.; Akbarov, K.; Abdel-Wahab, M. The Role of the Radiation Oncologist in Quality and Patient Safety: A Proposal of Indicators and Metrics. *Crit. Rev. Oncol. Hematol.* **2020**, *154*, 103045.
(25) Chaput, G.; Regnier, L. Radiotherapy: Clinical Pearls for Primary Care. *Can. Fam. Physician* **2021**, *67* (10), 753–757. https://doi.org/10.46747/cfp.6710753.
(26) Radiation Therapy Dosage. *News-Medical.net*. February 3, 2010. https://www.news-medical.net/health/Radiation-Therapy-Dosage.aspx (accessed 2022-10-20).
(27) Raman, C. V.; Krishnan, K. S. A New Type of Secondary Radiation. *Nature* **1928**, *121* (3048), 501–502. https://doi.org/10.1038/121501c0.
(28) Fleischmann, M.; Hendra, P. J.; McQuillan, A. J. Raman Spectra of Pyridine Adsorbed at a Silver Electrode. *Chem. Phys. Lett.* **1974**, *26* (2), 163–166. https://doi.org/10.1016/0009-2614(74)85388-1.
(29) Alessandri, I.; Lombardi, J. R. Enhanced Raman Scattering with Dielectrics. *Chem. Rev.* **2016**, *116* (24), 14921–14981. https://doi.org/10.1021/acs.chemrev.6b00365.
(30) Schlücker, S. Surface-Enhanced Raman Spectroscopy: Concepts and Chemical Applications. *Angew. Chem. Int. Ed.* **2014**, *53* (19), 4756–4795. https://doi.org/10.1002/anie.201205748.
(31) Pérez-Jiménez, A. I.; Lyu, D.; Lu, Z.; Liu, G.; Ren, B. Surface-Enhanced Raman Spectroscopy: Benefits, Trade-Offs and Future Developments. *Chem. Sci.* **2020**, *11* (18), 4563–4577. https://doi.org/10.1039/D0SC00809E.
(32) Wang, W.; Yin, Y.; Tan, Z.; Liu, J. Coffee-Ring Effect-Based Simultaneous SERS Substrate Fabrication and Analyte Enrichment for Trace Analysis. *Nanoscale* **2014**, *6* (16), 9588–9593.
(33) Wong, T.-S.; Chen, T.-H.; Shen, X.; Ho, C.-M. Nanochromatography Driven by the Coffee Ring Effect. *Anal. Chem.* **2011**, *83* (6), 1871–1873.

(34) Seo, C.; Jang, D.; Chae, J.; Shin, S. Altering the Coffee-Ring Effect by Adding a Surfactant-like Viscous Polymer Solution. *Sci. Rep.* **2017**, *7* (1), 500. https://doi.org/10.1038/s41598-017-00497-x.

(35) Lee, P. C.; Meisel, D. Adsorption and Surface-Enhanced Raman of Dyes on Silver and Gold Sols. *J. Phys. Chem.* **1982**, *86* (17), 3391–3395. https://doi.org/10.1021/j100214a025.

(36) Lord, cfRC; Thomas Jr, G. Raman Spectral Studies of Nucleic Acids and Related Molecules—I Ribonucleic Acid Derivatives. *Spectrochim. Acta Part Mol. Spectrosc.* **1967**, *23* (9), 2551–2591.

(37) Shalabaeva, V.; Lovato, L.; La Rocca, R.; Messina, G. C.; Dipalo, M.; Miele, E.; Perrone, M.; Gentile, F.; De Angelis, F. Time Resolved and Label Free Monitoring of Extracellular Metabolites by Surface Enhanced Raman Spectroscopy. *PLoS ONE* **2017**, *12* (4), e0175581. https://doi.org/10.1371/journal.pone.0175581.

(38) Sjöberg, B.; Foley, S.; Cardey, B.; Enescu, M. An Experimental and Theoretical Study of the Amino Acid Side Chain Raman Bands in Proteins. *Spectrochim. Acta. A. Mol. Biomol. Spectrosc.* **2014**, *128*, 300–311.

(39) Tang, H.-W.; Yang, X. B.; Kirkham, J.; Smith, D. A. Chemical Probing of Single Cancer Cells with Gold Nanoaggregates by Surface-Enhanced Raman Scattering. *Appl. Spectrosc.* **2008**, *62* (10), 1060–1069.

(40) Plou, J.; García, I.; Charconnet, M.; Astobiza, I.; García-Astrain, C.; Matricardi, C.; Mihi, A.; Carracedo, A.; Liz-Marzán, L. M. Multiplex SERS Detection of Metabolic Alterations in Tumor Extracellular Media. *Adv. Funct. Mater.* **2020**, *30* (17), 1910335. https://doi.org/10.1002/adfm.201910335.

(41) *Hypoxanthine - an overview | ScienceDirect Topics*. https://www.sciencedirect.com/topics/neuroscience/hypoxanthine (accessed 2023-02-20).

(42) Yin, J.; Ren, W.; Huang, X.; Deng, J.; Li, T.; Yin, Y. Potential Mechanisms Connecting Purine Metabolism and Cancer Therapy. *Front. Immunol.* **2018**, *9*, 1697. https://doi.org/10.3389/fimmu.2018.01697.

(43) Wu, K.; Ma, J.; Bai, W.; Cui, X.; Han, T.; Wang, S.; Xie, Y.; Xie, Y. Short-Term Intratracheal Use of PEG-Modified IL-2 and Glucocorticoid Persistently Alleviates Asthma in a Mouse Model. *Sci. Rep.* **2016**, *6* (1), 31562. https://doi.org/10.1038/srep31562.

(44) Elumalai, S.; Managó, S.; De Luca, A. C. Raman Microscopy: Progress in Research on Cancer Cell Sensing. *Sensors* **2020**, *20* (19), 5525. https://doi.org/10.3390/s20195525.

(45) De Gelder, J.; De Gussem, K.; Vandenabeele, P.; Moens, L. Reference Database of Raman Spectra of Biological Molecules. *J. Raman Spectrosc. Int. J. Orig. Work Asp. Raman Spectrosc. High. Order Process. Also Brillouin Rayleigh Scatt.* **2007**, *38* (9), 1133–1147.

(46) Notingher, I. Raman Spectroscopy Cell-Based Biosensors. *sensors* **2007**, *7* (8), 1343–1358.

(47) Kneipp, J.; Kneipp, H.; Wittig, B.; Kneipp, K. Novel Optical Nanosensors for Probing and Imaging Live Cells. *Nanomedicine Nanotechnol. Biol. Med.* **2010**, *6* (2), 214–226.

(48) Jeyavijayan, S.; Arivazhagan, M. Study of Density Functional Theory and Vibrational Spectra of Hypoxanthine. **2010**.

(49) Tanaka, K.; Choi, J.; Cao, Y.; Stacey, G. Extracellular ATP Acts as a Damage-Associated Molecular Pattern (DAMP) Signal in Plants. *Front. Plant Sci.* **2014**, *5*.

(50) Yegutkin, G. G. Nucleotide- and Nucleoside-Converting Ectoenzymes: Important Modulators of Purinergic Signalling Cascade. *Biochim. Biophys. Acta BBA - Mol. Cell Res.* **2008**, *1783* (5), 673–694. https://doi.org/10.1016/j.bbamcr.2008.01.024.

(51) Murao, A.; Aziz, M.; Wang, H.; Brenner, M.; Wang, P. Release Mechanisms of Major DAMPs. *Apoptosis* **2021**, *26* (3–4), 152–162. https://doi.org/10.1007/s10495-021-01663-3.

(52) Gafurov, M. M.; Kirillov, S. A.; Gorobets, M. I.; Rabadanov, K. Sh.; Ataev, M. B.; Tretyakov, D. O.; Aydemirov, K. M. Phase Equilibria and Ionic Solvation in the Lithium Tetrafluoroborate–Dimethylsulfoxide System. *J. Appl. Spectrosc.* **2015**, *81* (6), 912–918. https://doi.org/10.1007/s10812-015-0028-9.

(53) Chen, Z.; Coy, S. L.; Pannkuk, E. L.; Laiakis, E. C.; Hall, A. B.; Fornace, A. J.; Vouros, P. Rapid and High-Throughput Detection and Quantitation of Radiation Biomarkers in Human and Nonhuman Primates by Differential Mobility Spectrometry-Mass Spectrometry. *J. Am. Soc. Mass Spectrom.* **2016**, *27* (10), 1626–1636. https://doi.org/10.1007/s13361-016-1438-5.

(54) Johnson, C. H.; Patterson, A. D.; Krausz, K. W.; Kalinich, J. F.; Tyburski, J. B.; Kang, D. W.; Luecke, H.; Gonzalez, F. J.; Blakely, W. F.; Idle, J. R. Radiation Metabolomics. 5. Identification of Urinary Biomarkers of Ionizing Radiation Exposure in Nonhuman Primates by Mass Spectrometry-Based Metabolomics. *Radiat. Res.* **2012**, *178* (4), 328–340.